JGR Solid Earth

RESEARCH ARTICLE
10.1029/2021JB022539

# What Controls the Presence and Characteristics of Aftershocks in Rock Fracture in the Lab?

**Jörn Davidsen[1,2,3], Thomas Goebel[4,5], Grzegorz Kwiatek[2,6], Sergei Stanchits[7], Jordi Baró[1,8], and Georg Dresen[2,9]**

[1]Department of Physics and Astronomy, Complexity Science Group, University of Calgary, Calgary, AB, Canada, [2]Section 4.2: Geomechanics and Scientific Drilling, Helmoltz Centre Potsdam, GFZ German Research Centre for Geosciences, Potsdam, Germany, [3]Hotchkiss Brain Institute, University of Calgary, Calgary, AB, Canada, [4]University of Memphis, Center for Earthquake Research and Information, Memphis, TN, USA, [5]University of California, Santa Cruz, CA, USA, [6]Free University Berlin, Berlin, Germany, [7]Skolkovo Institute of Science and Technology, Moscow, Russia, [8]Centre for Mathematical Research, Barcelona, Spain, [9]University of Potsdam, Potsdam, Germany

**Key Points:**

- Spatial localization of seismic events during fracture nucleation and crack propagation occurs without temporal (Omori-type) correlations
- Post-fracture stress relaxation processes and large-scale stress heterogeneities lead to aftershock triggering
- Compaction and double couple events play a dominant role for aftershock triggering in the lab

**Supporting Information:**

Supporting Information may be found in the online version of this article.

**Correspondence to:**

J. Davidsen,
davidsen@phas.ucalgary.ca

**Citation:**

Davidsen, J., Goebel, T., Kwiatek, G., Stanchits, S., Baró, J., & Dresen, G. (2021). What controls the presence and characteristics of aftershocks in rock fracture in the lab? *Journal of Geophysical Research: Solid Earth*, *126*, e2021JB022539. https://doi.org/10.1029/2021JB022539

Received 3 JUN 2021
Accepted 18 SEP 2021

**Abstract** Aftershock cascades are a characteristic feature of natural seismicity, but underlying mechanisms remain debated. Here, we experimentally explore the presence or absence of aftershocks during failure of intact rock and slip on newly created laboratory faults. We show that the overall activity increase and spatial localization of acoustic emission (AE) events during fracture nucleation occurs without temporal (Omori-type) correlations. Our analysis shows that this absence of aftershock sequences occurs even beyond peak stress and also when a macroscopic fracture has formed post peak-stress and propagates. Instead, aftershock triggering does occur during post-fracture stress relaxation along the newly created lab-fault and in the presence of large-scale stress heterogeneities, for example, imposed by a saw-cut notch. The detected aftershocks in these cases can be described by standard seismological relationships such as a modified Omori-Utsu relation and its associated inter-event time distribution and productivity relation. Moreover, AE within all experiments follow the Gutenberg-Richter relation, with smaller *b*-values for triggered events compared to non-triggered events. Performing full-moment tensor inversions, we find that seismic events with significant isotropic, compaction components play an important role for aftershock triggering. The resulting triggered events tend to have focal mechanisms similar to their trigger. Seismic events with predominant tensile components, on the other hand, show little evidence for aftershock triggering. This opens up a new perspective on aftershocks, going beyond not only the rate-and-state paradigm limited to purely frictional sliding or shear events but also the mainshock attribute paradigm where mainshock attributes control aftershock patterns.

**Plain Language Summary** When rock is sufficiently stressed, first small microfractures or mini-earthquakes occur before the rock ultimately breaks. These microfractures show many similarities with natural earthquakes at much larger scales suggesting that lab experiments can help us to understand at least some aspects of earthquake dynamics. Whether this is also true for aftershocks—earthquakes triggered by a preceding earthquake as often observed in nature—is an open question. Here, we investigate what the necessary conditions are to induce aftershock sequences during rock fracture in a controlled lab environment. We show that even at high stress levels pronounced aftershock sequences are typically not observable. Instead, we find that either the presence of large scale imperfections such as a notch in the rock sample is necessary to observe aftershocks before the sample breaks or one has to consider the period of relaxation after the sample breaks. We are able to establish the contribution of different types of microfractures to aftershock sequences and also show that the aftershock sequences in the lab share many statistical features with natural aftershocks.



## 1. Introduction

Failure of intact rock in the brittle domain has long been studied experimentally to better understand the mechanical properties of heterogeneous materials (Mogi, 2007). One pronounced characteristic close to dynamic failure along faults and macroscopic fracturing of intact rock samples is the increase in the overall seismic energy rate released by microfractures as measured by acoustic emissions (AE) (Baró & Davidsen, 2018; Baró et al., 2018; Main & Meredith, 1989; Ohnaka & Mogi, 1982; Scholz, 1968a; Vu et al., 2019).

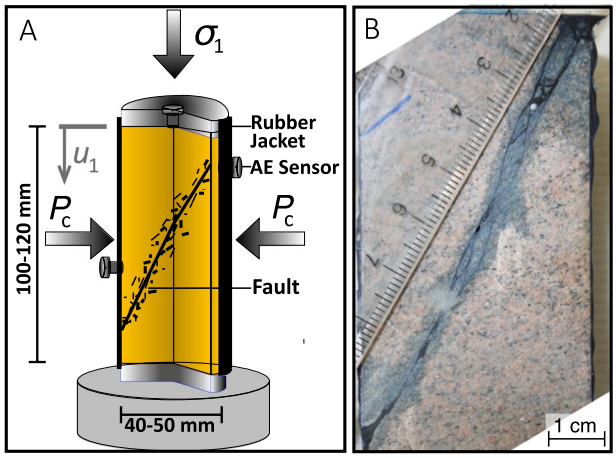


**Figure 1.** Overview of sample and fault geometry in the laboratory tests: The experimental setup is shown on the left and a picture of the fracture zone after failure for one of the Westerly granite samples (Wg01) is shown on the right.

This is accompanied by localization of the recorded microfractures along the future failure plane (Lennartz-Sassinek et al., 2014; Lockner et al., 1991). The co-occurrence of temporal and spatial correlations is a manifestation of an underlying damage localization process from isolated flaws to interacting flaws and finally macroscopic fracture as described in a plethora of studies (e.g., Lockner, 1993; Lockner et al., 1991; Peng & Johnson, 1972; Wong, 1982). The exact nature of these underlying interactions, however, remains an open question. One candidate for these interactions are internal relaxation processes in the form of seismic triggering such that the generation of one microfracture induces internal (static or dynamic or induced) stress changes throughout the sample (potentially) generating or activating multiple other microfractures afterward in a clear cause-and-effect scenario (Brodsky, 2006; Davidsen et al., 2017; Hainzl et al., 2014; Stein, 1999; van Der Elst et al., 2013; Velasco et al., 2008). In seismology, such a triggering process is generally assumed to be the cause of aftershock sequences both in the near-field and the far-field. The hallmark of such a seismic triggering process is that the activity is nonstationary giving rise to joint spatio-temporal correlations as described by the Omori-Utsu relation (Davidsen & Baiesi, 2016; Utsu et al., 1995). This relation captures the time-varying (local) seismic triggering rate following a given event, which asymptotically decays as a power-law with an exponent $p$ as empirically observed in nature and in the lab across a wide range of scales (Baró et al., 2013; Davidsen et al., 2015, 2017; Goebel et al., 2015; Gu et al., 2013; Maghsoudi et al., 2016, 2018; Mäkinen et al., 2015; Moradpour et al., 2014; Ribeiro et al., 2015; Utsu et al., 1995). Integrating the triggering rate over time gives the total number of triggered events by a given event, which on average increases with the size of that event as described by the productivity relation (Dascher-Cousineau et al., 2020; Davidsen & Baiesi, 2016; Gu et al., 2013; Marsan & Helmstetter, 2017; Schmid & Grasso, 2012; Wetzler et al., 2016). For tectonic earthquakes, these observations have led to the formulation of the statistical epidemic-type-aftershock sequence (ETAS) model and related ones (Davidsen & Baiesi, 2016; Holliday et al., 2008; Moradpour et al., 2014; Ogata, 1988; Zhuang et al., 2013), which separate the seismic activity rate $\mu(\vec{r},t)$ into a background rate $\mu_0$ — capturing the effect of the tectonic loading often assumed to be constant in space and time — and an aftershock rate — which is the sum over all space- and time-varying seismic triggering rates $\psi_i$ due to preceding earthquakes $i$ — such that $\mu = \mu_0 + \sum_i \psi_i$. Yet, recent rock fracture studies have shown that these seismic triggering processes are absent in initially intact samples under loading conditions mimicking those found in nature (Davidsen et al., 2017).

Here, we investigate experimentally to which extent this is also true at and beyond peak differential stress, to establish whether the previous observation generalizes to elevated stress levels, when the spatial localization of seismic events is particularly pronounced. We find that seismic triggering processes only start playing a significant role during post-fracture stress relaxation along the newly created lab-fault but not before — even if a macroscopic fracture has formed post peak-stress and propagates. Using an extensive suite of statistical methods, we compare the observed triggering to that arising in the presence of macroscopic imperfections in otherwise intact samples that is, notched samples before failure, and find no significant differences independent of the material and confining pressure. In particular, the behavior of the seismic triggering processes largely follows the same relations as tectonic aftershocks in nature suggesting their intrinsic scale-invariance.

## 2. Method and Experimental Set-Up

### 2.1. Loading Conditions and Sample Geometry

We present results from triaxial compression tests on five cylindrical ($r$ = 20–25 mm, $h$ = 100–120 mm) sandstone and granite samples. All samples were tested at room temperature and dry-ambient conditions, using a rubber jacket to separate the specimen and surrounding oil, which was used to apply confining pressures $P_c$ between 20 to 75 MPa (Figure 1). Deformation and seismic data during triaxial loading was

**Table 1**
*List of Triaxial Compression Experiments ($\sigma_2 = \sigma_3 < \sigma_1$) and Selected Time Windows for Triggering Analysis*

| Name | Large-scale imperfection | $\dot{u}$ ($\mu$m/min) | $P_c(\sigma_2 = \sigma_3)$ (MPa) | $m_{th}$ | $T_i$ (s) | $T_f$ (s) | $N$ |
|---|---|---|---|---|---|---|---|
| Wg01P | – | AE feedback | 75 | 2.35 | 8,200 | 8,350 | 1,283 |
| Wg01PF | – | 0 | 75 | 2.35 | 8,373 | 8,837 | 509 |
| WgN07 | notch | 20 | 75 | 2.35 | 0 | 5,825 | 8,114 |
| Ag73PP | – | AE feedback | 20 | 3.05 | 13,500 | 13,840 | 1,422 |
| AgN01 | notch | 20 | 20 | 2.25 | 0 | 2,400 | 2,291 |
| Fb33PP | – | AE feedback | 40 | 2.6 | 7,144 | 8,950 | 3,664 |
| Fb33CP | macro-crack | AE feedback | 40 | 2.4 | 9,020 | 9,450 | 634 |

*Note.* Here $\dot{u}$ is the displacement rate, $P_c$ is the confining pressure, $m_{th}$ is the AE magnitude of completeness, $T_i$ is the beginning of the observation period, and $T_f$ its end. $N$ is the number of AE events above $m_{th}$ during that period.

recorded from strain gauges and AE sensors attached directly to the rock surface. We measured the remotely applied force during constant displacement-rate loading ($\dot{u} = 20\ \mu m/min$) using a load cell. In addition to the experiments run at constant displacement-rate, we studied fracture initiation and propagation using an automatic AE-feedback loading system similar to Lockner et al. (1991). Depending on the AE event rate, we gradually reduced the loading rate; in the case of significant AE activity, we even stopped axial loading, and if AE activity was still sufficiently high, we removed some of the applied load to limit the elastic energy supply available for fracture propagation close to failure. The use of such an automatic feedback system leads to a very smooth approach to the specimen failure, extending the stage of macroscopic fault propagation to hours, making it possible to study the post-peak deformation of the specimen in detail (Stanchits et al., 2011).

We studied AE activity before, during, and after fracturing five rock samples (AgN01, Ag73, Fb33, Wg01, and WgN07). Compressive loading at elevated confining pressures resulted in the formation of localized fracture zones in all experiments. Samples were loaded until failure of intact and precut specimens. The latter contained 15 mm deep, saw-cut notches at a 30° angle to the loading axis (see Supporting Information S1). These notches guided the fracture process and allowed the investigation of the role of geometric heterogeneity on triggering behavior. The two notched (N) samples included one Aue granite (AgN01) and one Westerly granite (WgN07) (Goebel et al., 2012, 2014) specimen. The three intact samples included also one Aue granite (Ag73) (Davidsen et al., 2007; Stanchits et al., 2006) and one Westerly granite (Wg01) (Goebel et al., 2012, 2014) specimen. We tested the influence of lithology on triggering processes by also including porous Flechtingen sandstone (Fb33) with a porosity in the range 5.5–9% (Stanchits et al., 2011). In addition to varying initial geometry and lithology, the experiments were performed at different confining pressures (see Table 1). In all cases, the AE activity associated with axially loaded samples was used to characterize microfracturing processes using seismic moment tensors and polarity analysis (e.g., Kwiatek, Charalampidou, & Dresen, 2014; Kwiatek, Goebel, & Dresen, 2014). The observed kinematics of AE events (tensile opening, compaction, and shearing) was compared with triggering properties extracted from the AE catalogs.

### 2.2. Acoustic Emission Monitoring

The AE activity was recorded using a 16-channel acquisition system operating at 10 MHz sampling rate (Stanchits et al., 2006). This continuous acquisition with high sampling rate allowed for accurate AE event detections including their locations (see Appendix A–C for details) even when the AE activity was high during the failure process. AE events were processed in fixed time windows of 1,024 samples, such that the shortest time interval between two consecutive AE events equaled 102.4 $\mu$s in the experiments considered here. Yet, the P-wave onset times of AE arrivals at each particular channel were determined with accuracy of about 0.5 $\mu$s.

The AE magnitude was calculated as (Kwiatek, Goebel, & Dresen, 2014):

$$m = \log_{10}\sqrt{\frac{1}{n}\sum_{j=1}^{n}\left(A_j D_j\right)^2}, \quad (1)$$

where $A_j$ is the maximum amplitude of the first P-wave pulse detected at sensor $j$ corrected for the distance $D_j$ between the hypocenter of AE event and the sensor. We identified the magnitude of completeness $m_{th}$ as the lowest magnitude threshold for which the estimate of the $b$-value in the GR distribution became constant (Davidsen et al., 2015). As a note of caution, we would like to stress that a direct comparison of $b$-values measured at the lab scale to those measured at tectonic scales is not appropriate given the differences in the definition of magnitude.

Based on earlier calibration procedures (Zang et al., 1998), the AE kinematics can be quickly assessed using the polarity coefficient:

$$p = \frac{1}{N}\sum_{i=1}^{N}\text{sign}(A_i) \quad (2)$$

where $\text{sign}(A_i)$ is the polarity of the first P-wave pulse amplitude $A_i$ extracted from $N$ sensors. The polarity $p$ is used to categorize AE events into that displaying predominantly shear- ($-0.25 < p < 0.25$), tensile- ($p \geq 0.25$) or compaction-type ($p \leq -0.25$) mechanism (note that contrary to Zang et al., 1998 we reverted the sign convention, and associated $p = 1$ with tensile opening and $p = -1$ with compaction). The polarity method provides a good first order estimate of differences in AE source types because of the favorable sensor geometry and good focal coverage in the experiments (Zang et al., 1998).

The proportion of tensile versus compaction dominated AE events is strongly affected by confining pressure, sample porosity, and differential stress. High-porosity samples such as Flechtingen sandstone and high confining pressures promote more compaction events due to pore space collapse. Enhanced compaction is also observable in post-slip phases (Kwiatek, Goebel, & Dresen, 2014). Low confining pressures promote more-frequent shear and tensile-type events, which is further enhanced by increased differential stress. In addition, fault roughness can strongly affect focal mechanism heterogeneity with smooth faults showing more shear-type components and rough faults more isotropic components (Goebel et al., 2017); see also Figure 6 and associated discussion in (Dresen et al., 2020).

To further investigate the properties of the AE events, we calculated full moment tensor (FMTs) solutions (see Appendix A–C for details). For each FMT calculated, we used the diagonal elements $C_{ii}$ of the $6 \times 6$ covariance matrix of the six MT components as a quality constraint. Events with a maximum standard deviation of moment tensor components, $\sigma_{Mii,max} = \max\left\{\sqrt{(C_{ii})}\right\}$, less than a certain percentage of their seismic moment, $M_0$ (Kwiatek et al., 2016), were qualified for further processing. In cases where only a low number of seismic events were available, we chose a higher $\sigma_{Mii,max}/M_0$ threshold. The range of thresholds is $4\% - 10\%$, see Table 3 for details as well as Table S1 in the Supporting Information S1.

The accepted FMTs were decomposed into isotropic (ISO), compensated linear vector dipole (CLDV), and double-couple (DC) parts using the standard FMT decomposition scheme presented in (Knopoff & Randall, 1970). Using the FMT decomposition, we categorize AE event kinematics into tensile (ISO $\geq 15\%$ and CLVD $\geq -15\%$), compaction (ISO $\leq -15\%$ and CLVD $\leq 15\%$), and non-volumetric or shear ( ISO$| < 15\%$) events. FMTs with ISO and CLVD outside of the defined areas (i.e., ISO $> 15\%$ and CLVD $< -15\%$ or ISO $< -15\%$ and CLVD $> 15\%$) were rejected from further analysis, as the FMTs with opposite signs of ISO and CLVD components are considered unphysical (less than 4% of FMTs have been removed in this step, see Table 3 for details) (Vavryčuk, 2001).

To establish the focal mechanism similarity between specific events, we also calculate the 3D rotation angles $\delta$ between their cardinal $P$ (pressure) and $T$ (tension) axis directions of their FMTs (Kagan, 2007). Here, $\delta < 20°$ suggests comparable fault kinematics. For specific subsets of AE events, we also calculated the median rotation angle, $\tilde{\delta}_{50} = \text{median}\left\{\delta_i\right\}$ between all possible pairs of focal mechanisms to provide a simple comparative measure of focal mechanism similarity between the different subsets. Time-constrained subsets of processed catalogs of AE activity associated with each experiment (cf., Table 1) are provided in the associated data publication (Goebel et al., 2021).

### 2.3. Changes in Stress, Acoustic Emission Rates and Spatial Localization

For our experiments, Figures 2 and 3 show the typical rapid increase in AE rates toward the point of dynamic failure, which coincides with a pronounced peak in AE activity and drop in differential stress. Since all experiments were carried out at room temperature and dry conditions as well as the same constant loading rate, applying AE-feedback control only close to failure, we can rule out that temperature, pore pressure as well as differently applied stresses lead to differences in the AE rates between the different experiments. Instead the AE rates in our experiments are related to the level of differential stress and damage history of the sample. Pre-failure stages are characterized by increasing AE rates resulting from accelerating crack development and interaction. For the initially intact samples, the increase in AE activity close to failure coincides with a clear spatial localization of events as shown, for example, in Figure 2. Due to the AE feedback controlled loading, this behavior can be extended beyond the peak loading stress. Spatial localization becomes even more pronounced once a macro-crack has formed and started to propagate subcritically as the example of Fb33CP in Figure 2 shows. A similar level of spatial localization of AE events is evident during the post-failure relaxation period as exhibited by Wg01PF in Figure 2.

Spatial localization of AE events also occurs in notched samples — with the main difference that this happens even far away from peak stress. Figure 3 provides a clear example of this. The AE activity is mostly clustered along the tip of the notch as expected.

### 2.4. Temporal Correlations and Event-Event Triggering

To test whether the observed spatial localization of activity across different experiments and different periods is related to aftershock triggering or more precisely event-event triggering, that is, the direct triggering of an event by a preceding event due to static, dynamic, or induced stress changes (without considering whether the trigger is larger or smaller than the triggered event as in the aforementioned statistical ETAS model framework), we now focus on the temporal and spatio-temporal properties of the AE activity in more detail. Specifically, we use two different and well-established measures to test the hypothesis that the temporal properties of the AE events arise from a Poisson process, that is, a random process without any temporal memory between subsequent events. Such a process is fully determined by the rate of events, which might or might not vary with time.

The first measure focuses on the interevent time ratio $R$ (Davidsen et al., 2017; van der Elst & Brodsky, 2010), which is defined as $R_i = \frac{\Delta t_{i+1}}{\Delta t_i + \Delta t_{i+1}}$ for any given event $1 < i < N$. Here, $\Delta t_i$ is the time interval between event $i$ and $i-1$. For both stationary and time-varying Poisson processes, the probability density function (PDF) of $R$ is uniform in the interval from 0 to 1. Given the number of AE events $N$, one can establish significant bounds for this PDF. A significant peak at $R = 0$ suggests triggering, since the occurrence of an event tends to lead to a shorter than expected time interval until the next event. A significant peak at $R = 1$ indicates quiescence or anti-clustering, since the occurrence of an event tends to lead to a longer than expected time interval until the next event. We test the effects of two conditioning methods by only selecting (a) triggers above a specific magnitude, and (b) subsequent events with specific magnitude differences $\delta_m$. For (a), as large events are expected to trigger other events more frequently, the peak at 0 should become more pronounced if $R_i$ is conditioned on events with larger magnitudes $m_i$, indicated by $m > m_{min}$ in the following. For (b), as overlapping triggering sequences might be present, one can minimize their effect by conditioning on the magnitude difference between subsequent events such that only values of $R_i$ are considered, for which $m_i > m_{i-1}$, indicated by $\delta_m = 0.0$ to 0.6 in the following. If the condition is not met there is a higher chance that event $i-1$ might have triggered event $i+1$.

The second measure we use, here referred to as Bi-test (Baró et al., 2014; Bi et al., 1989), also focuses on interevent time ratios but considering time symmetry. Following the convention used for the $R$-test, we define the variable $\Delta\tau_i$ as the shortest interevent value around $i$: $\Delta\tau_i = \min(\Delta t_i, \Delta t_{i+1})$. We will also consider $\Delta\tau_i^+$ as the following interevent time in the same temporal directions, that is, we can either obtain $\Delta\tau_i = \Delta t_i$ and $\Delta\tau_i^+ = \Delta t_{i-1}$ or $\Delta\tau_i = \Delta t_{i+1}$ and $\Delta\tau_i^+ = \Delta t_{i+2}$, depending on the temporal direction of the closest event to $i$. If the interevent values $\Delta t$ arise from a Poisson process — even with smooth temporal variations in its rate — the statistics of $\Delta\tau^+$ are independent of $i$ and, thus, equally distributed as for a Poisson process. We

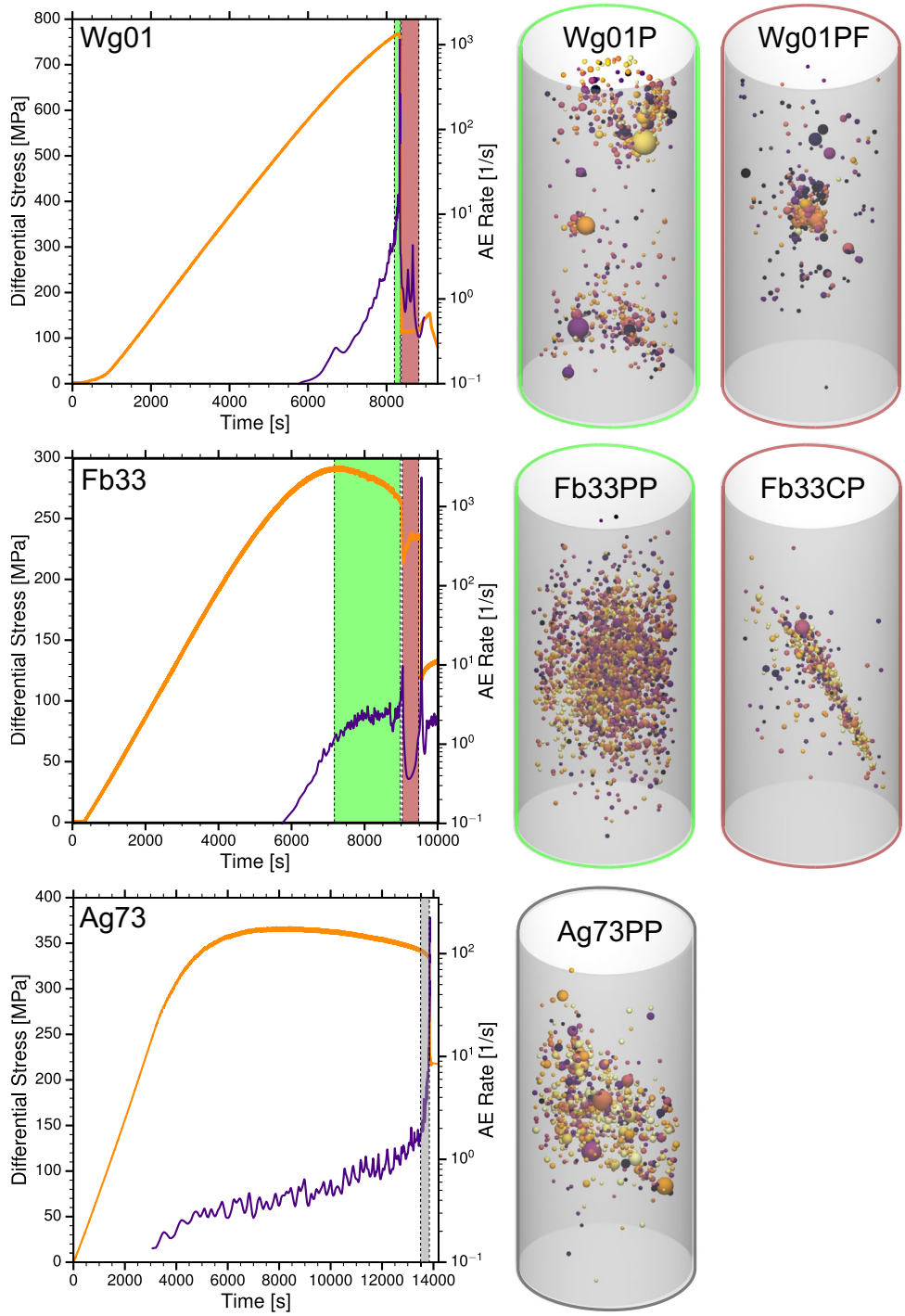


**Figure 2.** Overview of the experiments on initially intact samples: Westerly granite Wg01 (first row), Flechtingen sandstone Fb33 (second row), and Aue granite Ag73 (third row). Temporal evolution of differential stress (orange) and acoustic emissions (AE) activity (purple) is shown in the first column. The colored areas highlight the different periods around and beyond peak stress selected for the triggering analysis (see also Table 1). The right-hand columns show the locations of the AE events during these periods using the same color contours for the respective frame. The size of the spheres corresponds to the AE event magnitude. The color of the spheres reflect the time of occurrence within a given time period (see also Table 1), with earlier and later times marked with darker and lighter colors, respectively. In all cases, a clear spatial localization of events is visible (see also the Supporting Information S1 for different views). Note that in the third column, the locations of the AE events during the post-failure (PF) relaxation period are shown, denoted by Wg01PF, and beyond peak stress in the presence of crack propagation (CP), denoted by Fb33CP.

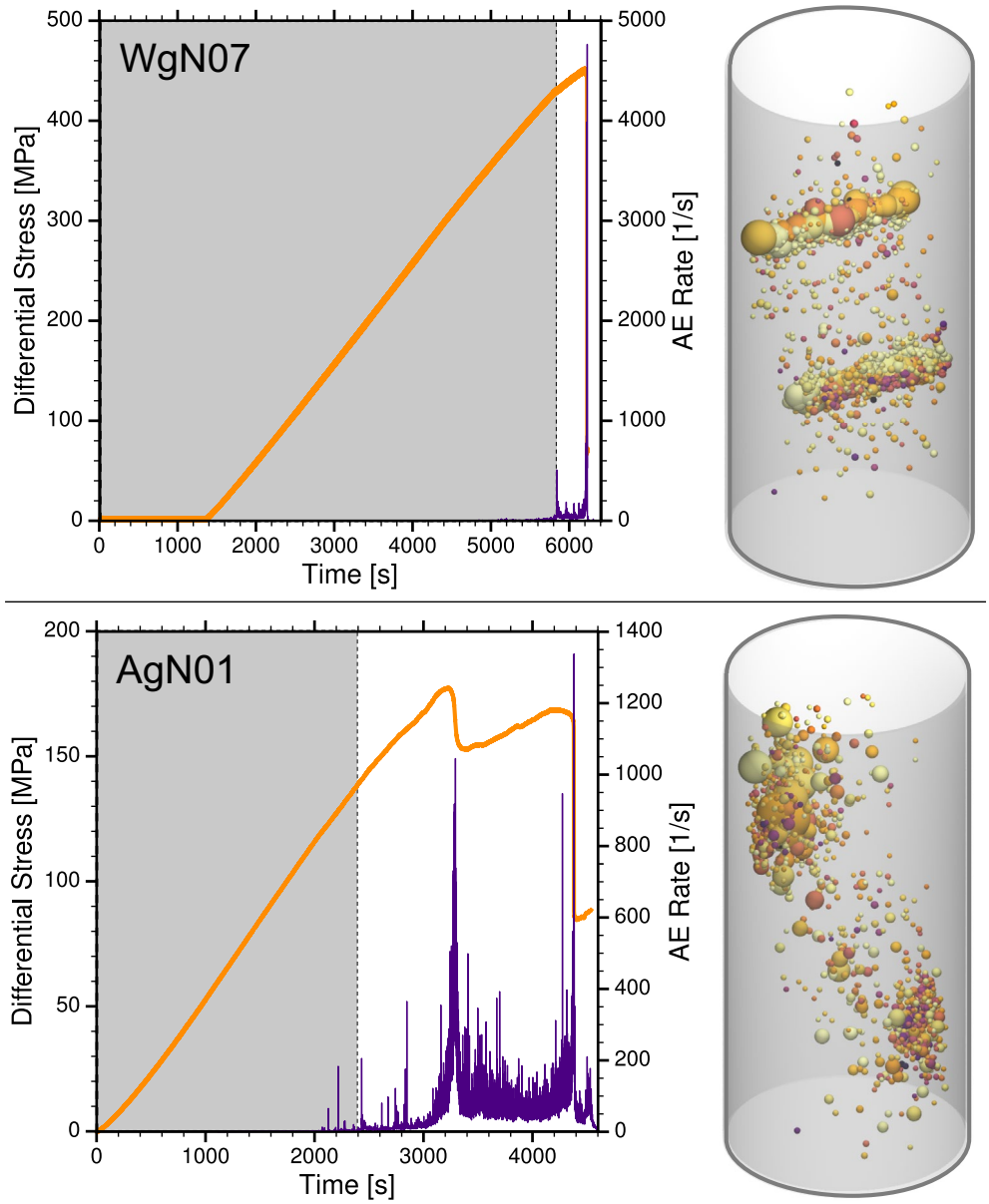


**Figure 3.** Overview of the experiments as in Figure 2 but for notched samples: Westerly granite (WgN07) (top row), and Aue granite (AgN01) (bottom row). A photo of AgN01 together with the different views can be found in the Supporting Information S1.

define the statistical variable $H_i = \Delta\tau_i/(\Delta\tau_i + 0.5\Delta\tau_i^+)$. Similarly to $R$, the values of $H$ are uniformly distributed between 0 and 1 when the process is Poissonian. In the case of $H$, both clustering and anti-clustering lead to an excess of $H$ values around 0 and 1. For a large number ($N$) of $H$ values, the difference between the cumulative distribution ($F_N(H)$) and the Poisson null-model prediction ($F(H) = H$) is indicative of the behavior: When the intervals are more regular than expected in a Poisson process, the profile of the difference ($(F_N(H) - H)$) renders a significant (see Appendix A–C for details) 90° clockwise rotated "S" shape. Clustering is identified as a 90° counter-clockwise rotated "Z" shape (Baró et al., 2014).

The reason why we use two different measures to test the hypothesis that the temporal properties of the AE events arise from a Poisson process is that the $R$ statistics also allows one to distinguish between triggering and anti-clustering due to the time directionality, while the Bi-test allows one to distinguish directly between regularity and irregularity, where the latter can imply clustering or anti-clustering.

Finally, to explicitly test for seismic triggering and the presence of aftershocks, we follow exactly the same well-established statistical approach as Davidsen et al. (2017) and Zaliapin et al. (2008), for example (see also Gu et al., 2013; Zaliapin & Ben-Zion, 2013). This "declustering" method does not simply rely on inter-event times as the previous two methods, but instead it takes into account the full space-time-magnitude information. In a nutshell, the method compares the observed local rate of activity to the one expected based on the global rate of activity as captured by the Gutenberg-Richter relation (Gutenberg & Richter, 1949), while taking into account the variation of the latter with the considered spatio-temporal window of interest. Thus, it tests the hypothesis whether the spatiotemporal activity is consistent with a homogeneous spatio-temporal Poisson process for a given magnitude. Significant deviations are interpreted as triggering relationships between pairs of events: The earlier event is labeled as the unique trigger (cause) of the later event (effect). In this approach, a given event can have at most a single trigger but the number of events it triggers itself is in principle unlimited. Specifically, for a given event $j$, one identifies the lowest local rate expected based on the global Gutenberg-Richter relation by

$$n_j^* = \min_{i<j} \left\{ (r_{ij})^{D_f} t_{ij} 10^{-bm_i} \right\}, \tag{3}$$

where $r_{ij}$ is the spatial distance, and $t_{ij}$ is the temporal distance between events $i$ and $j$. The parameters $b$ and $D_f$ are the $b$-value of the Gutenberg-Richter relation and the (fractal) spatial dimension of the observed AE activity, respectively, which can be estimated independently. The $b$-values are given in Table 4 and we use $D_f = 2.3$ throughout (Davidsen et al., 2017) since our findings do not sensitively depend on the specific value of $D_f$, consistent with previous studies (Davidsen et al., 2015). Triggered events are those for which $n_j^*$ is very low, events for which $n_j^*$ is high are considered to be background events, consistent with the ETAS model framework. The corresponding threshold value $n^*$ can be established by considering randomized versions of the AE catalog where time, location, and magnitudes are shuffled independently (Davidsen et al., 2017). Typically, a mix of triggered events and background events are expected to lead to a bimodal distribution of $n_j^*$ and the threshold $n^*$ attempts to separate the two populations (Davidsen et al., 2017; Zaliapin et al., 2008) though this cannot be done perfectly (Bayliss et al., 2019).

### 2.5. Triggering Cascades and Event-Event Interactions in the Lab and in Nature

Analogous to many studies of natural seismicity, we evaluate the presence or absence of aftershock triggering of microseismic events based on spatial-temporal proximity of event pairs, while taking magnitudes into account as well (see Section 2.4). This classification is based solely on a statistical assessment of clustering characteristics without requiring ad-hoc choices of space-time windows. Similarly, no specific triggering mechanisms are assumed, analogous to cluster analysis of natural earthquakes (e.g., Reasenberg, 1985). Although the statistical treatment of AE events mirrors natural seismicity studies, underlying source processes may be different. Source mechanisms in the laboratory, represented with MTs, encompass both isotropic and deviatoric components. This includes shear, shear-tensile failures (shear faulting with associated positive volumetric change due material displacement), or intensive comminution of displaced materials after the slip of the macroscopic fault plane, expressed in dominance of pore collapses, or shear-compaction processes. The observed processes occur at grain-scale and they are dependent on ambient stress magnitude, deviatoric stress evolution ("earthquake cycle"), and roughness of the fault surface (e.g., Charalampidou et al., 2014; Goebel et al., 2017; Kwiatek, Goebel, & Dresen, 2014; Stanchits et al., 2006; Zang et al., 1998). Such processes are more difficult to resolve in nature due to the lack of high-frequency monitoring (cf., Kwiatek & Ben-Zion, 2013, 2016), which negatively synergize with the expected lower radiation of high-frequency seismic waves from non-shear ruptures. It may also be that non-shear processes are more prominent at smaller laboratory scales (cf., Kwiatek, Charalampidou, & Dresen, 2014), but it is overall difficult to relate each dynamic AE event and its kinematics to the actual microstructural changes. Note that the differences in laboratory source types may also lead to more complex event-event interactions. A more detailed discussion of triggering mechanisms in lab and nature is provided in Section 4.3.

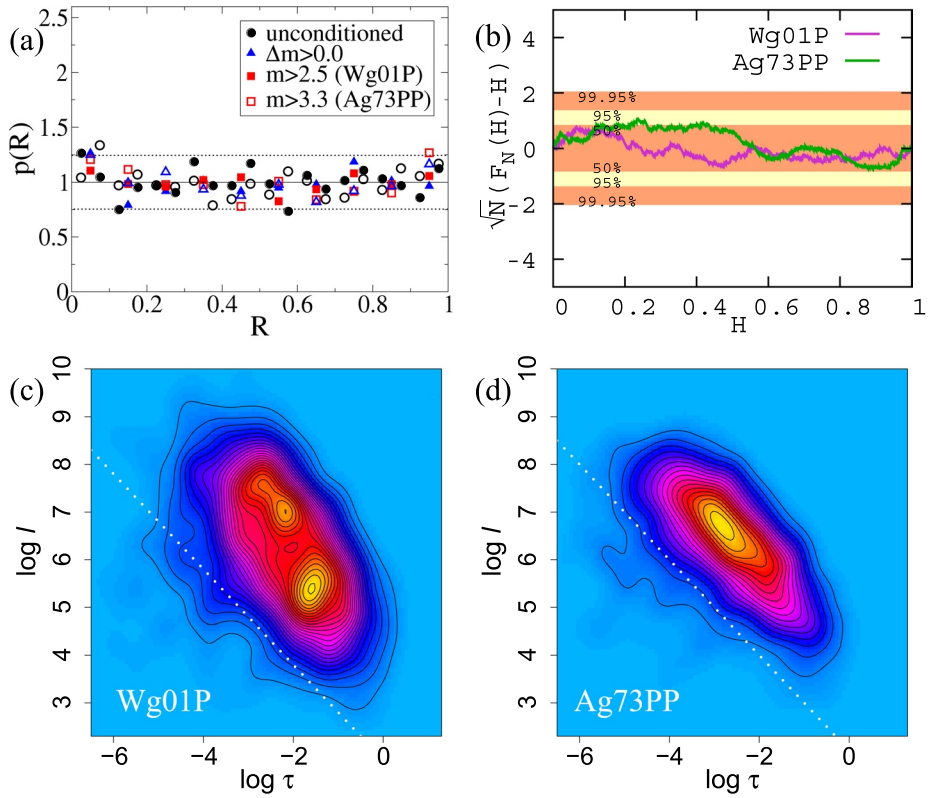


**Figure 4.** Triggering analysis for Westerly granite peak stress (Wg01P) and Aue granite post peak stress (Ag73PP): (a) Probability density function (PDF) of the interevent time ratio $R$ for different conditions, see main text for details. Solid symbols correspond to Wg01P, open symbols to Ag73PP. The dotted lines correspond to the 95% confidence intervals of a uniform distribution (based on Poissonian errors) for the unconditioned case of Wg01P. In all other cases, the uncertainties are as least as large. Since almost all data points are within the 95% confidence intervals, we cannot reject the hypothesis of a Poisson process at high confidence. (b) Kolmogorov-Smirnov (KS) test for the distribution of the $H$ statistics obtained by the Bi-test. In both cases, the $p$-values cannot reject the Poisson hypothesis, given by the relation $F_N(H) = H$, at the $\approx$ 50% confidence interval. (c) and (d) Density plots of the set $\{n_j^*\}$ represented in $\log \tau - \log l$ space with $\tau_j^* = t_j^* 10^{-bm_i^{*}/2}$ and $l_j^* = (r_j^*)^{D_f} 10^{-bm_i^{*}/2}$ such that $n_j^* = \tau_j^* l_j^*$. Data are denser in yellow regions and tend to zero density in blue regions. Distances are measured in millimeters and time is measured in seconds. The threshold $n^*$ is shown as the straight line in the plots, which separates the two different populations of triggered events (below the line) and background events (above the line). There is minimal evidence for triggering in both cases.

## 3. Results

We focus on the series of experiments described above with different initial conditions and fault stress level to test the presence and strength of triggering in triaxial compression tests. We start by analyzing initially intact samples prior to failure and during stable fracture propagation. We compare these tests with results from slip on incipient faults at low differential stress. Lastly, we investigate the effect of large macroscopic notches that concentrate stresses at the end of the notches.

### 3.1. Initially Intact Samples Before Brittle Failure

We first focus our analysis on the granite samples Wg01 and Ag73, which are initially intact. Specifically, we focus on the AE activity close to and at peak stress (Wg01P) and post peak stress (Ag73PP), see Figure 2 and Table 1. In both cases, all three measures of triggering indicate a minimal amount or absence of triggering as shown in Figure 4. This is despite the fact that the $b$-value decreases close to failure while measures of spatial localization increase at the same time (see, e.g., Figure S5 in the Supporting Information S1). These are typically interpreted as signs of the onset of nonlocal interactions between cracks (e.g., Lockner, 1993). For the temporal correlations, the $R$ and the Bi-test indicate that the hypothesis of a Poisson process (stationary

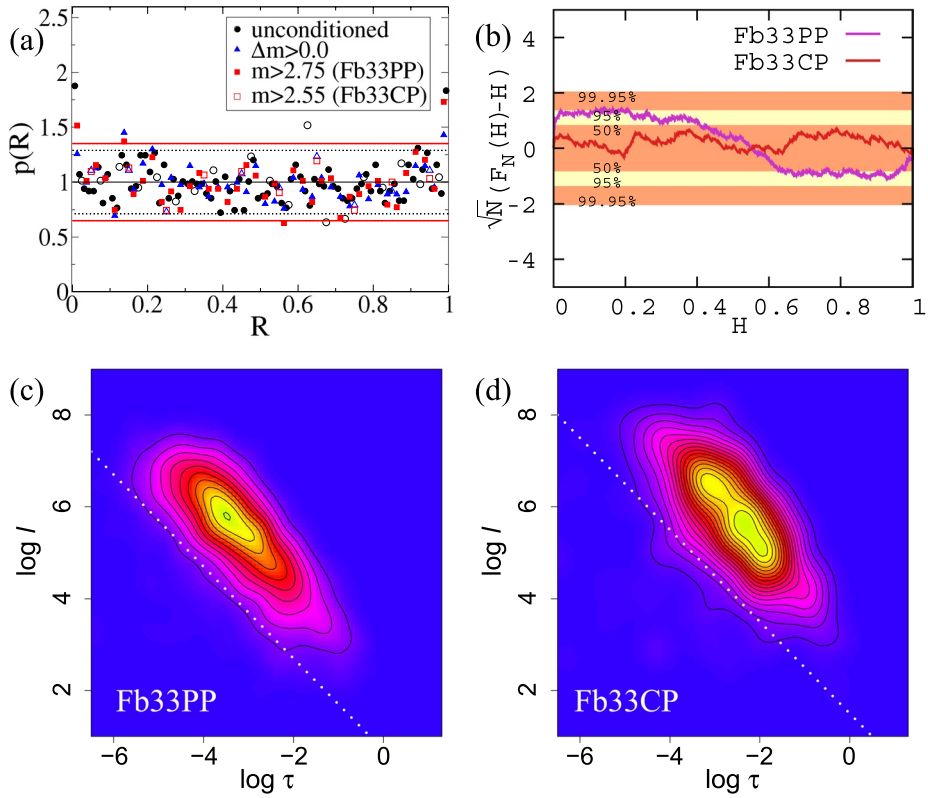


**Figure 5.** Triggering analysis as in Figure 4 but for Fb33PP and Fb33CP. (a) Probability density function (PDF) of the interevent time ratio $R$ for different conditions. Solid symbols correspond to Fb33PP, open symbols to Fb33CP. The dotted lines correspond to the 95% confidence intervals for the unconditioned case of Fb33PP, and the solid red lines are for the $m > 2.55$ case of Fb33CP. In all other cases, the uncertainties are in between those two. (b) Kolmogorov-Smirnov (KS) test of the $H$ values obtained by the Bi-test. The $p$-values cannot reject the Poisson hypothesis at the 50% level in the case of Fb33CP. For Fb33PP, the Poisson hypothesis is just rejected at the ≈ 95% level. The profile resembles the rotated "Z" shape characteristic of clustering. (c) and (d) Density plots indicating that the number of triggered events below the line is minimal.

or non-stationary) cannot be rejected at the 95% confidence level. For direct event-event triggering, we find an absence of a clear bimodality in the density plots. In addition, the estimated percentage of triggered events or aftershocks is low, not more than about 5% (Ag73PP) and 5% (Wg01P), respectively.

A similar behavior can be observed in the case of the sandstone sample FB33, which is also initially intact. The triggering analysis for the AE activity post peak stress (Fb33PP, see Figure 2 and Table 1) and beyond peak stress in the presence of crack propagation (Fb33CP, see Figure 2 and Table 1) is shown in Figure 5. For the temporal correlations, the Bi-test indicates that the hypothesis of a Poisson process cannot even be rejected at the 50% confidence level during crack propagation (Fb33CP). The R-test for Fb33CP shows that conditioning further strengthens the null hypothesis of a Poisson process as not a single deviation beyond the 95% confidence level remains. Yet, for Fb33PP the situation is a little bit different. The Bi-test rejects Poissonian behavior just at the ≈ 95% confidence interval. The unconditional R-test exhibits a significant peak close to $R = 0$ and close to $R = 1$. While the former peak could be indicative of triggering, it becomes less significant in the conditional R-test using $m > 2.75$ and insignificant using $\Delta m > 0$. Both observations suggest that the peak at $R = 0$ is not a consequence of triggering but rather related to short-term catalog incompleteness. On the other hand, the peak at $R = 1$ remains significant even in the conditional R-tests indicating the presence of anti-clustering such that shorter and longer interevent times tend to alternate, even if the event in the middle is larger than the previous one. For direct event-event triggering, we find again no bimodality in the density plots making a clear identification of triggered events challenging. The estimated percentage of triggered events is again low and not more than about 3% (Fb33PP) and 4% (Fb-33CP), respectively.

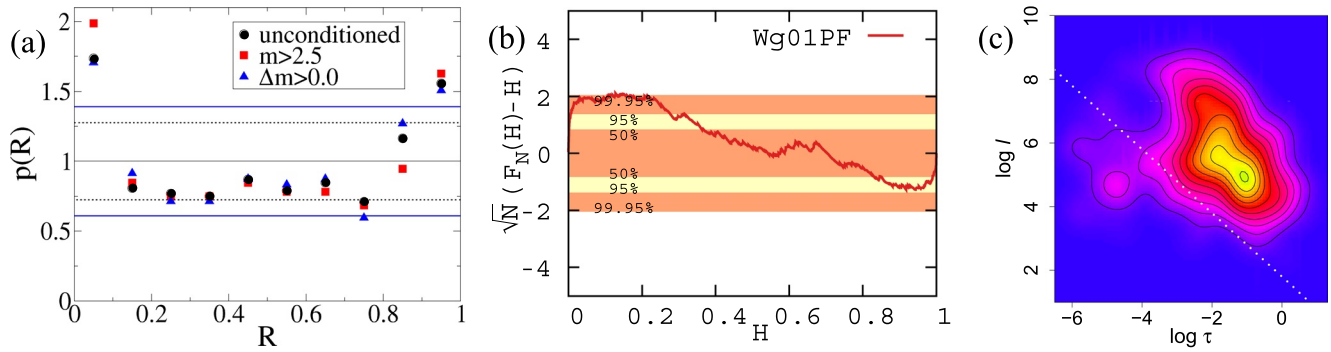


**Figure 6.** Triggering analysis as in Figure 4 but for post-failure relaxation period of the initially intact granite sample Wg01 (Wg01PF). (a) Probability density function (PDF) of the interevent time ratio $R$ for different conditions. The dotted lines correspond to the 95% confidence intervals for the unconditioned case, and the solid blue lines are for the $\Delta m > 0.0$ case. In the other case, the uncertainty is in between those two. The significant deviation close to $R = 0$ indicates triggering. (b) The Kolmogorov-Smirnov (KS) test over the $H$ values from the Bi-test rejects the Poisson hypothesis at 99.95%. The rotated "Z" shape denotes clustering. (c) Density plot showing a clear sign of bimodality.

### 3.2. Post-Failure Relaxation Period of Initially Intact Sample

Next, we analyze the AE activity during the post-failure relaxation period of the initially intact granite sample Wg01 (Wg01PF), see Figure 2 and Table 1. In contrast to the previous cases, all three measures of triggering indicate a substantial amount of triggering as shown in Figure 6. For the temporal correlations, the $R$ and the Bi-test indicate that the hypothesis of a Poisson process can be rejected at a confidence level higher than the 99% level. Specifically, the $R$-test shows a significant peak at $R = 0$, which becomes more pronounced if one conditions on larger magnitudes $m$. This is exactly what one expects in the presence of triggering. A smaller, less significant peak at $R = 1$ is also present. For direct event-event triggering, we find bimodality in the density plots as expected in the presence of triggering and the estimated percentage of triggered events is about 10%.

### 3.3. Notched Samples at Stress Levels Below the Peak Stress

We now test the effect of large, artificial heterogeneities on triggering potential prior to failure. Figures 7 and 8 summarize the triggering analysis for the notched granite samples WgN07 and AgN01 at stress levels below the peak stress (see Figure 3 and Table 1). Similar to the case of post-failure relaxation, all three measures indicate triggering as shown in Figures 7 and 8, yet at an even higher level for both samples. For the temporal correlations, the $R$ and the Bi-test indicate that the hypothesis of a Poisson process can be rejected at a confidence level higher than the 99.95% level. Specifically, the $R$-test shows a significant peak at $R = 0$, which becomes more pronounced if one conditions on larger magnitudes $m$. This is exactly what one expects in the presence of triggering. A slightly smaller but still significant peak at $R = 1$ is also present. For direct event-event triggering, we find signs of bimodality in the density plots as expected in the presence of triggering. The estimated average percentage of triggered events or aftershocks is about 11% (AgN01) and 13% (WgN07), respectively. Note that this percentage can significantly increase over time as, for example, shown in Table 2 for AgN01, where it increases from about 7% at early times to about 15% at later times despite being far from failure. The similarity in triggering percentages between the two notched samples indicates that the slightly larger spectrum of grain sizes for Aue granite compared to Westerly granite alone does not seem to have much effect on triggering.

### 3.4. Relation Between Stress Level, AE Source Types, and Triggering

To investigate possible relationships between event-event triggering and AE event kinematics, we now focus on the analysis of AE source types, starting with source-type distinctions based on polarity information. For the Westerly granite samples, the AE events during the selected time periods we focus on are dominated by events arising from compaction-type mechanism as a result of the high confining pressures (Table 2) as discussed in Section 2.2. However, this is not the case for Aue granite and Flechtingen sandstone loaded at lower confinement, where shear-type and tensile-type mechanisms play significant roles. Notably, in all cases

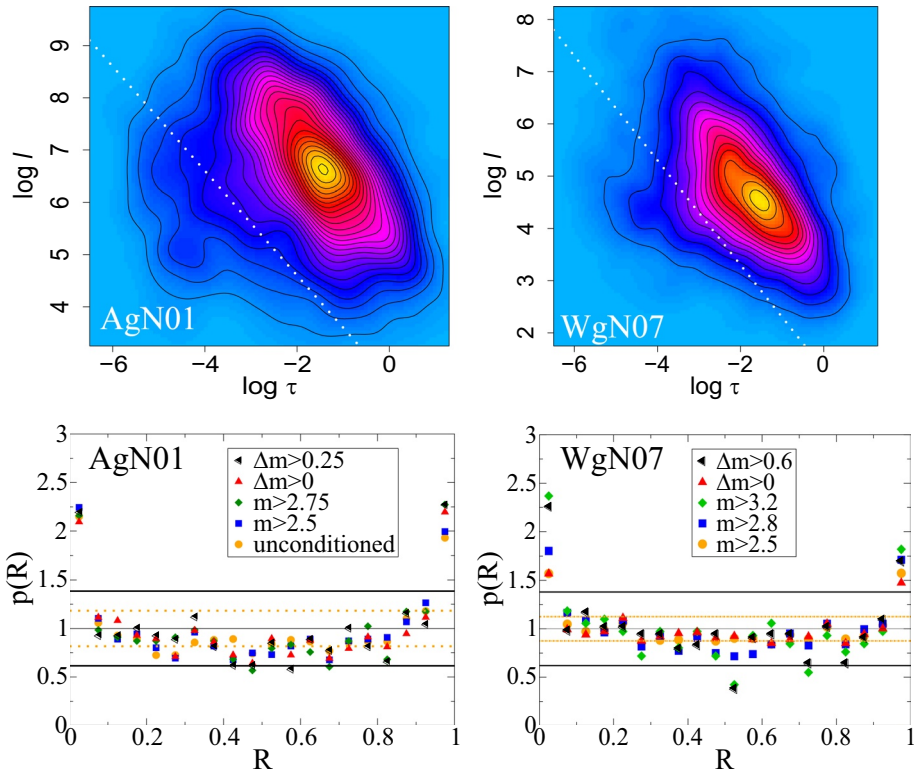


**Figure 7.** Triggering analysis for Aue granite (AgN01) (left column) and Westerly granite (WgN07) (right column). Top row: Density plots as in Figures 4c and 4d. Bottom row: Probability density function (PDF) of the interevent time ratio $R$ for different conditions as in Figure 4a. The thick solid and dotted lines correspond to the 95% confidence intervals for the largest $\Delta m$ threshold and the smallest $m$ threshold (or the unconditioned case as indicated by color), respectively. These correspond to the largest and smallest uncertainties of all data sets shown in a panel. The significant deviation close to $R = 0$ indicates triggering.

where event-event triggering occurs, triggered events exhibit a much higher percentage of compaction-type events whereas background events (events that are not triggered by other events) show a reduced percentage of compaction events. In contrast, the percentage of tensile-type source components is reduced for triggered events and elevated for background events. It is important to point out that an overall dominance of compaction-type mechanisms does not guarantee triggering, see Wg01P and Fb33CP (Table 2 and Figures 4 and 5). Similarly, a lack of dominance of compaction-type mechanisms does not prevent event-event triggering, see AgN01 (Table 2 and Figures 8 and 7). In addition, AgN01 shows that triggered events are not necessarily dominated by compaction-type mechanisms, at least at early times when shear-type mechanisms occur more often, and also when compared to background events.

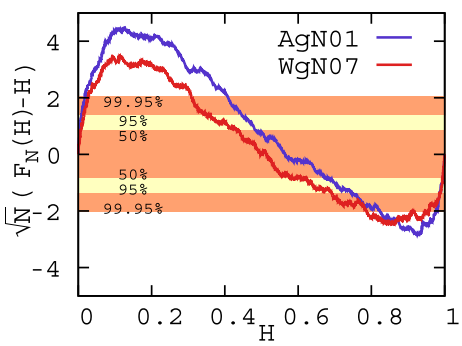


**Figure 8.** Kolmogorov-Smirnov (KS) test over the $H$ values obtained by the Bi test for Aue granite (AgN01) and Westerly granite (WgN07) as in Figure 4b. For both samples, the $p$-values show that the clustering is significantly above the 99.95% confidence interval, clearly rejecting the Poisson hypothesis. The 90° counter-clockwise rotated "Z" shape indicates clustering.

We further test the robustness of the influence of source types on triggering characteristics by examining moment tensor solutions and decomposing the source tensor into isotropic, double couple, and CLVD components. This decomposition can be visualized in a Hudson plot (Hudson et al., 1989; Vavryčuk, 2014) with good agreement between moment tensor decomposition and average polarity information (Figure 9), similar to the agreement found in a related study (Graham et al., 2010). The different source type categories based on moment tensor decomposition again highlight relatively lower percentages of tensile events in triggered event populations whereas compaction-type events are elevated compared to background (Table 3). A key observation from the moment

**Table 2**
*AE Event Kinematics (Compaction-Type, Shear-Type and Tensile-Type Mechanisms) Based on the Polarities (Equation 2)*

| Name | (sub-) set | Number | Compaction | Shear | Tensile |
|---|---|---|---|---|---|
| Wg01P | all | 1,283 | 61% | 28% | 11% |
| Wg01PF | all | 509 | 79% | 18% | 3% |
| Wg01PF | trigger | 51 | 90% | 10% | 0% |
| Wg01PF | triggered | 67 | 91% | 9% | 0% |
| Wg01PF | background | 442 | 77% | 19% | 4% |
| WgN07 | all | 8,114 | 68% | 24% | 8% |
| WgN07 | trigger | 842 | 78% | 21% | 1% |
| WgN07 | triggered | 1,113 | 77% | 21% | 2% |
| WgN07 | background | 7,001 | 66% | 24% | 10% |
| Ag73PP | all | 1,422 | 19% | 71% | 10% |
| AgN01 | all | 2,291 | 23% | 38% | 39% |
| AgN01 | trigger | 174 | 45% | 34% | 21% |
| AgN01 | triggered | 291 | 47% | 37% | 16% |
| AgN01 | background | 2,000 | 20% | 38% | 42% |
| AgN01-1st | all | 1,000 | 15% | 36% | 49% |
| AgN01-1st | trigger | 49 | 18% | 51% | 31% |
| AgN01-1st | triggered | 77 | 27% | 47% | 26% |
| AgN01-1st | background | 923 | 14% | 35% | 51% |
| AgN01-2nd | all | 1,291 | 30% | 39% | 31% |
| AgN01-2nd | trigger | 125 | 55% | 28% | 17% |
| AgN01-2nd | triggered | 214 | 55% | 33% | 12% |
| AgN01-2nd | background | 1,077 | 25% | 40% | 35% |
| Fb33PP | all | 3,664 | 39% | 35% | 26% |
| Fb33CP | all | 634 | 65% | 25% | 10% |

*Note*. For AgN01 these are also given for the first 1,000 events and for the remaining 1,291 events separately.

tensor analysis is the high similarity of seismic moment tensors between a triggered event and its trigger, with median rotation angles between 14 and 16° (Table 3). In contrast, background events show a much higher level of heterogeneity of focal mechanism solutions with median rotation angles between 59 and 71°.

### 3.5. Event-Event Triggering: Temporal Characteristics and Productivity Relation

In order to establish additional properties of the underlying processes responsible for event-event triggering in our experiments, we now focus on temporal aspects such as the triggering rates, that is, the rate of occurrence of triggered events at a given moment in time after a potential trigger. As Figure 10 shows for WgN07, there are two different regimes: At early times these rates decay as a power law with an exponent $p \approx 0.7$ similar to the Omori-Utsu relation, and at later times they decay more rapidly, namely as a power law with an exponent ≈ 1.8. The number of triggered events in our other two catalogs that show triggering (AgN01 and Wg01PF) is unfortunately too small to give a reliable estimate of the triggering rates. Yet, if triggering is present one can use the interevent time distribution to recover the early time regime and the associated $p$.

To do so, we consider the previous definition of an interevent time $\delta_i = \Delta t_i = t_i - t_{i-1}$ as the time interval between subsequent events above a given magnitude threshold $M$. Figure 11 shows the distribution of interevent times for the samples exhibiting triggering, that is, WgN07, AgN01, and Wg01PF, and different thresholds, scaled by the average interevent-time of each series ($\langle\delta\rangle(M)$). We observe a collapse of the scaled distribution to a single universal curve $f(\theta)$ such that $P(\delta) \sim f(\delta/\langle\delta\rangle)/\langle\delta\rangle$. In all cases, a power-law can be observed for short waiting times (short-dashed red lines). We fitted the corresponding exponents by a double-logarithmic linear regression for $\delta < 0.3\langle\delta\rangle$. The fitted exponents range from $0.49 \pm 0.02$ to $0.77 \pm 0.02$. In the presence of triggering, these exponents are fully determined by $p$ and their values are given by $2 - 1/p$ (Corral, 2003; Shcherbakov, Turcotte, & Rundle, 2005; Utsu et al., 1995). Inverting this relation, the interevent-time distributions give $p$ in the range $0.66 \pm 0.01$ to $0.81 \pm 0.02$. Within the statistical uncertainties, these values agree with the directly estimated value of $p = 0.7 \pm 0.1$ for WgN07 in Figure 10. The existence of a stationary background rate of independent events would return an exponential cut-off in the distribution for long interevent times in Figure 11 (green line). On the contrary, long interevent times are, in all cases, better fitted by a power-law with a steep exponent $\nu$ (long-dashed red lines) ranging from $1.78 \pm 0.04$ to $2.10 \pm 0.12$. Only the post-failure example with triggering (Wg01PF) is still compatible with an exponential cutoff due to low statistics. While one could naively expect the second power-law regime for long interval times to be a consequence of the second power-law regime in the triggering rates observed for WgN07 (with an exponent $1.8 \pm 0.1$, see Figure 10), the two associated power-law exponents are not consistent with one another (Baró & Davidsen, 2017). Yet, such a power-law decay for long interevent times is expected in the presence of a nonstationary background rate (Baró & Davidsen, 2017; Corral, 2003), which is consistent with our experiments.

The interevent time distributions for the catalogs that do not show event-event triggering behave in a significantly different way as Figure 12 shows. The scaling functions for Fb33PP, Fb33CP, Ag73PP, and Wg01P, are well fitted by a generalized Gamma function: $f(\theta) \approx \text{gen.}\,\Gamma(\theta;\gamma,\beta) \sim \frac{|\beta|\exp(-\theta^{\beta})}{\theta^{1-\gamma}\Gamma(\gamma/\beta)}$, where $\Gamma(z) := \int_{\mathbb{R}^+} t^{z-1}\exp(-t)dt$. The positive parameters $\gamma$ and $\beta$ control the scaling function for short and long

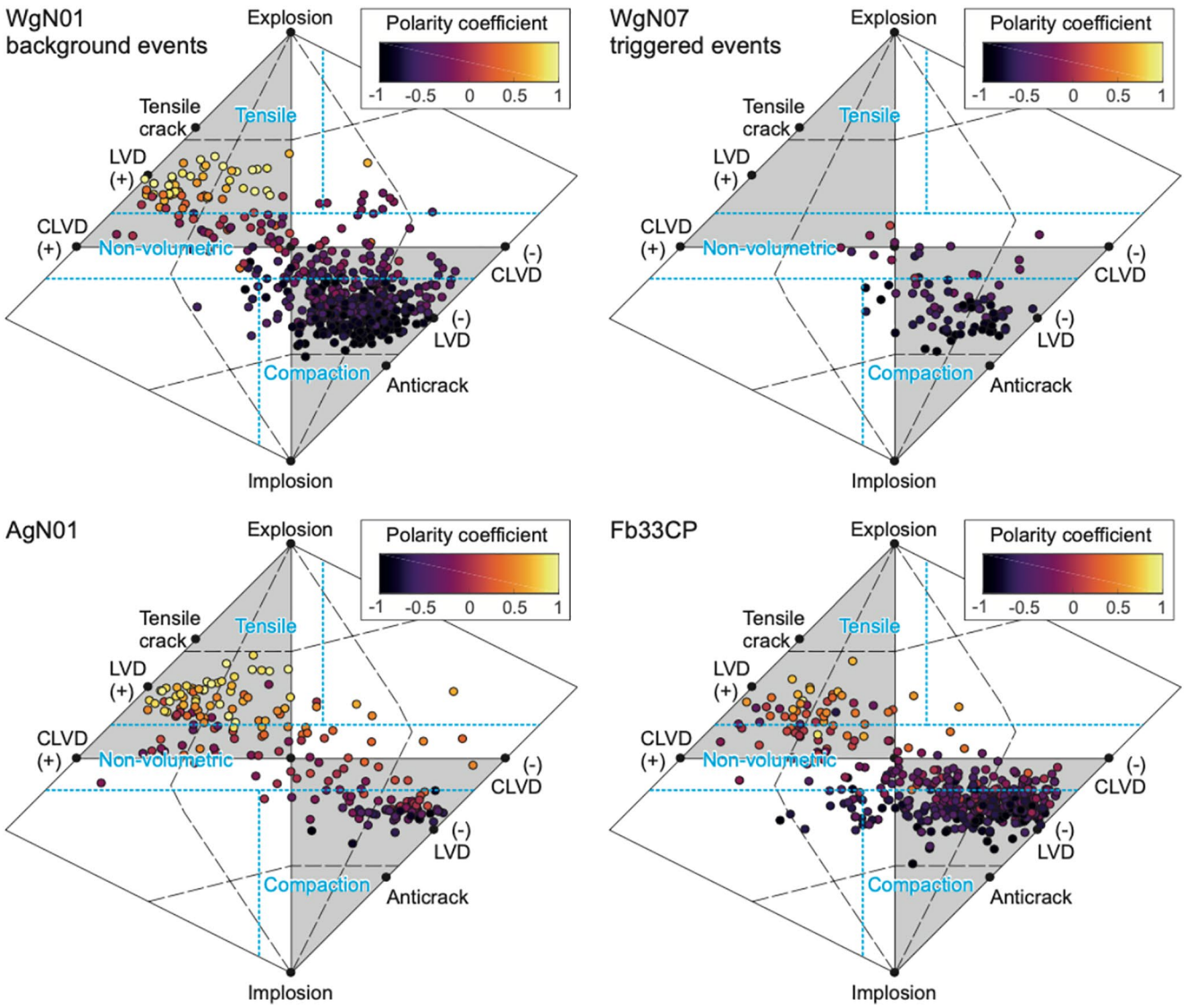


**Figure 9.** From left to right, top to bottom: (i) Hudson equal-area plot for Westerly granite (WgN07), background events only, (ii) WgN07, triggered events only, (iii) Aue granite (AgN01), and (iv) Fb33CP. The separation into volumetric and non-volumetric kinematics is presented with dashed blue lines (see also Table 3). The faulting kinematics characterized by polarity coefficient (cf., 2) is color-encoded with −1.0 and 1.0 corresponding to pure compaction-type and tensile-type events, respectively.

interevent times, respectively. For Fb33PP and Fb33CP, $\beta = 0.9$ and $\gamma = 1.0$, such that they are close to an exponential function expected for a homogeneous Poisson process. In contrast, the overall scaling function for the distributions of Ag73PP and Wg01P clearly departs from the exponential form — predominantly at small arguments — and is better fitted by the generalized Gamma function with significantly lower exponents: $\beta = 0.7$ and $\gamma = 0.7$. This might indicate temporal variations in the underlying point process. Since the triggering analysis had shown compatibility with a local Poisson process (Figure 4), we argue that the discrepancies from the homogeneous Poisson are caused by the strong temporal variations (up to 3 decades) in the activity rate observed in the post-peak regime (see Figure 2).

Finally, integrating the triggering rate of an event of magnitude $M$ over time gives rise to a productivity relation for the number of events triggered by such an event. The right panel in Figure 10 shows the productivity relation for WgN07 and AgN01 (the number of triggered events for Wg01PF is too small to give a reliable estimate). In both cases, we find for the average $\langle N \rangle(m) \propto 10^{\alpha m}$ with $\alpha \approx 1.1 - 1.2$ corresponding to a self-similar increase in the number of triggered events with the magnitude of the trigger.

**Table 3**
*Classification of AE Event Kinematics Based on the FMTs Decomposition Into Tensile-Type, Compaction-Type, and Shear-Type Mechanism, See the Corresponding Hudson Plots in Figure 9 for Comparison*

| Name | (sub-) set | $N_{total}$ | $N_{mt}^{initial}$ | $N_{mt}^{final}$ | $\frac{\sigma_{Mii,max}}{M_0}$ | Compaction | Shear | Tensile | $\tilde{\delta}_{50}$ |
|---|---|---|---|---|---|---|---|---|---|
| WgN07 | all | 8,114 | 611 | 595 | <0.04 | 69% | 21% | 10% | 58° |
| WgN07 | triggered | 1,113 | 86 | 86 | <0.04 | 78% | 22% | 0% | 16° |
| WgN07 | background | 7,001 | 525 | 509 | <0.04 | 67% | 21% | 12% | 59° |
| AgN01 | all | 2,291 | 196 | 193 | <0.1 | 36% | 28% | 36% | 67° |
| AgN01 | triggered | 291 | 33 | 33 | <0.1 | 94% | 3% | 3% | 14° |
| AgN01 | background | 2,000 | 163 | 160 | <0.1 | 24% | 33% | 43% | 71° |
| AgN01-1st | all | 1,000 | 92 | 92 | <0.1 | 22% | 30% | 48% | 70° |
| AgN01-2nd | all | 1,291 | 104 | 101 | <0.1 | 49% | 26% | 25% | 65° |
| Fb33PP | all | 3,664 | 2,942 | 2,895 | <0.1 | 36% | 37% | 27% | 68° |
| Fb33CP | all | 634 | 425 | 411 | <0.1 | 60% | 30% | 10% | 64° |

*Note*. The total number of AE events, initial, and final number of FMTs calculated are $N_{total}$, $N_{mt}^{initial}$, and $N_{mt}^{final}$, respectively. The quality criteria are discussed in the main text, see also Table S1 in the Supporting Informatin S1 for a robustness analysis. The median rotation angle $\tilde{\delta}_{50}$ for background and all events was calculated for a set of rotation angles calculated in-between all possible pairs of focal mechanisms forming the subset. For triggered subset, $\tilde{\delta}_{50}$ was calculated for a set of rotation angles calculated between mechanisms of triggered events and their corresponding trigger only.

### 3.6. Event-Event Triggering: Gutenberg-Richter Relation

Next, we analyze the frequency-magnitude distributions and their dependence on the selected events. While triggered and background AE events follow the Gutenberg-Richter relation across experiments, we find that both WgN07 and AgN01 exhibit different *b*-values for triggered and background AE events, see Figure 13. In particular, the *b*-value of 1.06 ± 0.03 for triggered events is significantly smaller than for background events with $b = 1.54 \pm 0.02$ for WgN07. The same trend holds for AgN01, where $b = 0.79 \pm 0.05$ for triggered events and $b = 1.38 \pm 0.03$ for background events. These differences in *b*-value do not vary much over time (certainly less so than measures of localization such as the fractal dimension (Hirata et al., 1987) and the correlation coefficient (Zang et al., 1998) despite some coevolution (Henderson et al., 1994), see Figures S3 and S4 in the Supporting Information S1) and hold for all AE source types (see Table S2 in the Supporting Information S1).

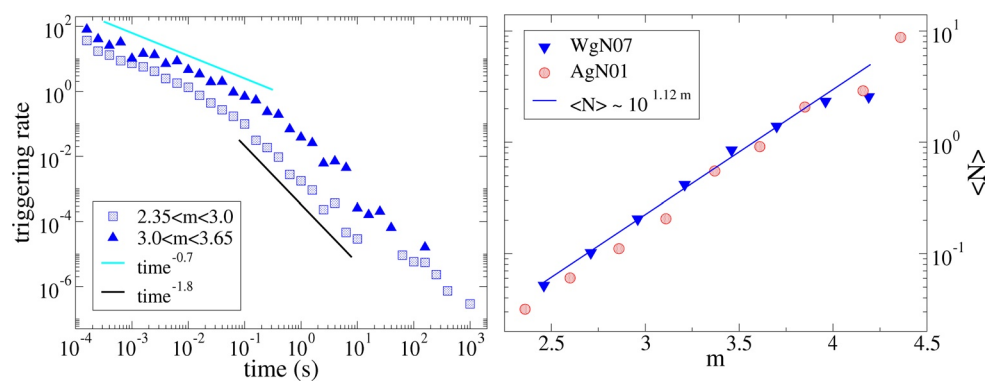


**Figure 10.** Left: Triggering rate for Westerly granite (WgN07) as a function of time after the time of occurrence of a trigger averaged over different magnitude ranges of the trigger or main shock. Rates are higher for larger magnitudes but the functional forms are basically identical. Right: Productivity relation for WgN07 and Aue granite (AgN01), indicating that on average an event with a larger magnitude *m* triggers more events *N*.

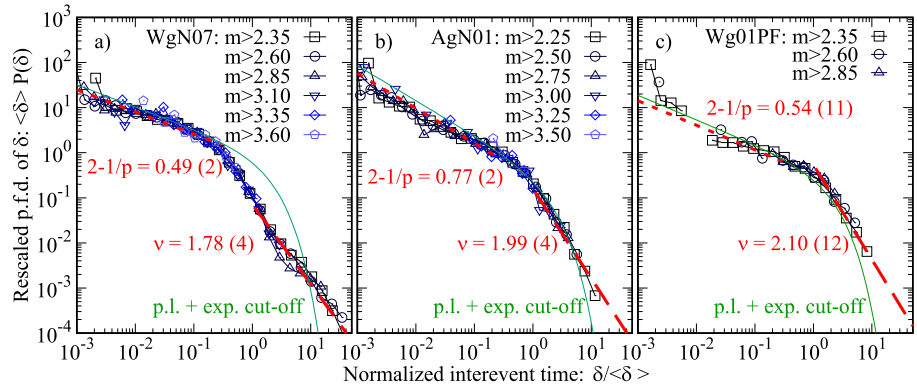


**Figure 11.** Westerly granite (WgN07), Aue granite (AgN01), and post-failure relaxation period of the initially intact granite sample Wg01 (Wg01PF) (left to right): Rescaled distributions of interevent times between AE events for different magnitude thresholds. For small arguments ($\delta < 0.3\langle\delta\rangle$) the distributions fit a power law (short-dashed red lines) with exponent – 0.49 ± 0.02 (WgN07), – 0.77 ± 0.02 (AgN01), and – 0.54 ± 0.11 (Wg01PF). For long interevent times, the distributions decay faster. Green lines represent a power-law with an exponential decay as expected for a constant background rate. Long-dashed red lines represent the best fit of a second power-law for $\delta > \langle\delta\rangle$, with steeper exponents $\nu$. The error bars are shown in brackets.

For comparison, we also include the estimated *b*-values for the other AE catalogs in Table 4. As one can see, the *b*-values for the catalogs that do not exhibit triggering are not systematically different from the ones that do, although *b*-values are low when only considering triggered events. For the Aue granite samples, the *b*-value of the sample with the notch (AgN01) is lower than for the one without (Ag73PP). For the Westerly granite samples, the opposite is true: Wg01P has a smaller *b*-value than WgN07 and also than Wg01PF.

Finally, we also find that there are typically significant variations in *b*-values with AE source type (Table S2 in the Supporting Information S1). Tensile events tend to display higher *b*-values, e.g., $b = 1.87 \pm 0.12$ for tensile events and $b = 1.38 \pm 0.04$ for compaction events in WgN07, see Table S2 in the Supporting Information S1. We speculate this might be related to the fact that tensile events can be affected by grain size distribution, as the intragranular tensile crack is likely to stop at grain contacts, an intergranular crack likewise, thus limiting the size distribution of such cracks leading to the higher *b*-values typically observed. Accordingly, in highly compressive environments, as it is the case for all our experiments, creating a tensile opening is energetically demanding, limiting the radiation of seismic waves at the same time.

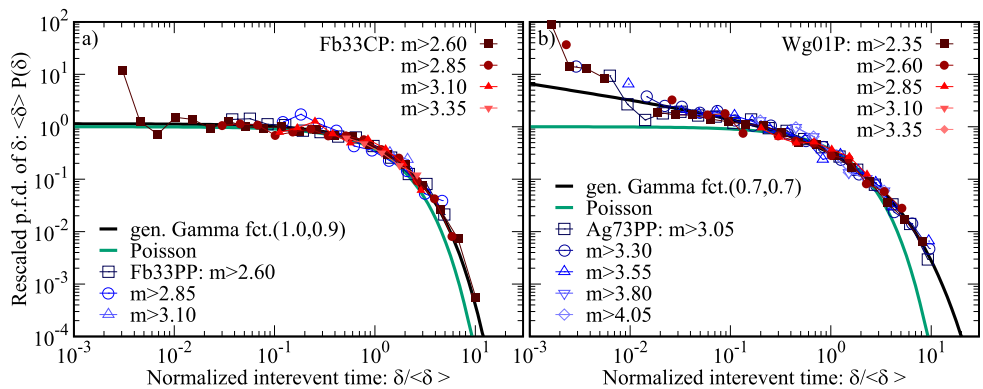


**Figure 12.** Fb33PP and Fb33CP (left) and Aue granite post peak stress (Ag73PP) and Westerly granite peak stress (Wg01P) (right): Rescaled distributions of interevent times between acoustic emissions (AE) events for different magnitude thresholds. Green line represents an exponential function, expected for a homogeneous Poisson processes. Black line represents the best fit for the generalized Gamma function, $\Gamma(\theta;\gamma,\beta)$. Differences from the homogeneous Poisson process are more prominent in Ag73PP and Wg01P, and the distributions are better fitted with $\Gamma(\theta;0.7,0.7)$, significantly different from an exponential.

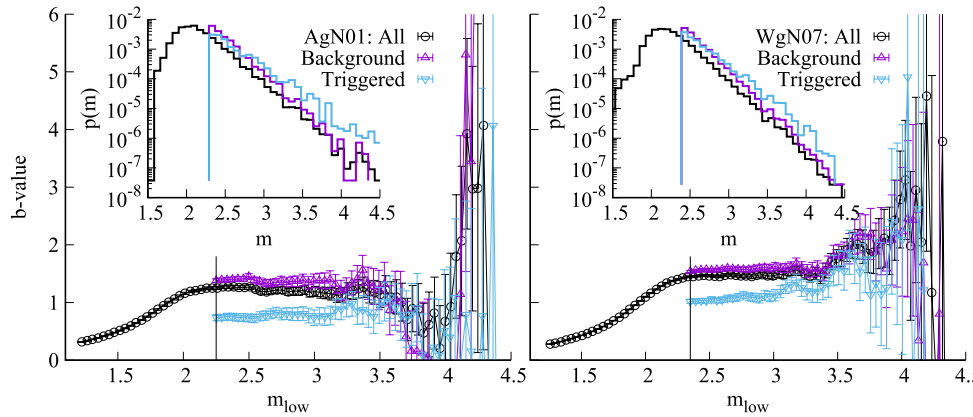


**Figure 13.** Westerly granite (WgN07) and Aue granite (AgN01): *b*-values estimated by maximum likelihood within the interval of magnitudes $m_{low} < m < \infty$ as a function of $m_{low}$. The catalogs are split in triggered and background events. The *b*-value for the distribution of triggered events is lower for both catalogs. WgN07: from $b = 1.540$ (18) with a goodness-of-fit *p*-value of 0.52 for background to $b = 1.06$ (3) with *p*-value 0.53 at $m_{low} = m_c$. AgN01: from $b = 1.38$ (3) with a *p*-value of 0.54 for background to $b = 0.79$ (5) with *p*-value 0.53 at $m_{low} = m_c$. Insets: Frequency-magnitude distributions.

## 4. Discussion

### 4.1. Factors That Govern Aftershock Triggering in Lab Experiments

An increase in the microcracking activity rates together with a spatial localization of microcracks before the ultimate failure of a heterogeneous material is a well-established phenomenon (e.g., Kun et al., 2014; Lennartz-Sassinek et al., 2014). Our analysis comprising a range of tri-axial compression experiments on sandstone and granite samples shows that the overall activity increase, spatial localization of AE events, and decreasing *b*-values during fracture nucleation are typically not indicative of seismic triggering processes and that the temporal correlations between AE events are trivial and can be well described by a nonhomogeneous Poisson process (e.g., Table 2 and Figures 4 and 5). In particular, this absence of seismic event-event triggering or aftershock sequences is not specific to lower stress levels (Davidsen et al., 2017) but we show for the first time here that this behavior occurs even around peak stress, as in Wg01P, as well as past peak stress, as in Fb33PP and Ag73PP, and even if a macroscopic fracture has formed post peak-stress and starts to propagate, as observed in the post-peak activity of the sandstone sample (Fb33CP). This indicates that while proposed models for the nucleation and growth of faults in intact brittle rocks based on the interaction of tensile microcracks (Reches & Lockner, 1994) might still be valid, these proposed interactions not only would have to be significantly different from those dominating during aftershock sequences but also would have to exhibit a temporal signature consistent with a nonhomogeneous Poisson process. This could arise, for example, through a more significant role of aseismic processes. Experimentally establishing the importance of aseismic processes in rock fracture remains a challenge for the future. Moreover, our findings imply that the suggested mechanisms for aftershock triggering in damage mechanics — visco-elastic effects (Baró & Davidsen, 2018; Ben-Zion, 2008; Nanjo et al., 2005; Zhang & Shcherbakov, 2016) or a broad distribution of characteristic times (Narteau et al., 2002; Scholz, 1968b) — either do not play an important role in the fracture of the samples we studied or simply do not lead to seismic triggering here.

On the contrary, seismic triggering does naturally occur during post-fracture stress relaxation along the newly created lab-fault as observed for the Westerly granite sample (Wg01PF) — where one might expect that friction rather than fracture is responsible for triggering—and in the presence of other large-scale stress heterogeneities, for example, imposed by a saw-cut notch as in the granite samples WgN07 and AgN01 (e.g., Table 2 and Figures 6–8). The latter is consistent with earlier findings, where it was also shown that a macroscopic imperfection such as a natural high density inclusion in a sandstone sample can facilitate event-event triggering (Davidsen et al., 2017). The importance of large-scale stress heterogeneities for the occurrence of seismic triggering is consistent with the picture that the local stress intensity, rather than the stress measured on the sample boundary, controls the susceptibility to triggering (Meredith & Atkinson, 1983).

**Table 4**
*b-Values Estimated by Maximum Likelihood Within the Interval of Magnitudes $m_c < m < \infty$ With Uncertainties Indicated in Brackets and the Associated p-Values Calculated Using the Deluca-Corral Method With 10,000 Synthetic Catalogs (Deluca & Corral, 2013) to Establish the Goodness-of-Fit*

| Name | *b*-value | *p*-value | Triggering |
|---|---|---|---|
| Wg01P | 1.38 (3) | 0.55 | no |
| Wg01PF | 1.47 (7) | 0.57 | yes |
| Ag73PP | 1.42 (4) | 0.55 | no |
| WgN07 | 1.452 (16) | 0.51 | yes |
| AgN01 | 1.27 (3) | 0.53 | yes |
| Fb33PP | 2.37 (4) | 0.56 | no |
| Fb33CP | 2.09 (8) | 0.62 | no |

*Note*. Figure 14 shows the variability of the *b*-value with the applied lower magnitude threshold. The last column summarizes which AE catalogs exhibit event-event triggering.

Since it is known that the interaction between a macroscopic crack and microcracks (AE events) leads to increased local stress fluctuations (Kachanov, 1994), our findings indicate that such fluctuations are necessary for aftershock triggering. Whether previously suggested visco-elastic effects or a broad distribution of characteristic times are required in addition, remains an open question. Although differences in rock microstructure may have an influence on triggering processes we could not determine it in the context of our (limited) experiments and it remains a challenge for the future. Instead our specific observations for granite and sandstone samples suggest that aftershock triggering in this case is governed by macro-scale dynamics. The experiments with Flechtingen sandstone, for instance, included a well-defined period of quasi-stable, macroscopic fracture propagation (Fb33CP) without seismic triggering. Seismic triggering was, however, associated with stress relaxation and slip on a freshly formed fault in Westerly granite (Wg01PF). These observations suggest that the dynamics of macro-scale processes rather than microstructure or differences in lithology led to triggering.

Our full-moment tensor analysis (e.g., Tables 2 and 3) shows that seismic events with significant isotropic, compaction components frequently play an important role for triggering. Seismic events with predominant tensile components, on the other hand, show little evidence for triggering. This novel insight indicates that the simple conceptual picture of purely frictional sliding or shear events often applied to understand triggering and aftershocks as, for example, in the rate-and-state paradigm (Heimisson & Segall, 2018) cannot be directly applied to the mechanisms involved in rock fracture under compression. It is important to realize that non-shear processes evidenced in the calculated MTs can be interpreted mostly as being indicative of shear-compaction or shear-tensile kinematics, which geologists may call "trans-pressional" or "trans-tensional," respectively, as observed on larger scales. This is because most of the events on the Hudson plots in Figure 9 cluster along the line that can be formally described with the shear-tensile MT model of Vavryčuk (2001). Mechanically, such shear-compaction mechanism may involve crushing via Hertz contacts (tensile) and shearing of grains or fragments to locally close a pore space. Thus, it is conceivable that compaction processes at the microscale could lead to an effective rate-and-state friction law such that the same mechanisms responsible for triggering in rock fracture could still be indirectly related to the original features of large-scale tribology. On a more general level, the observed relation between AE kinematics and their propensity for triggering could originate from spatial differences in local stress intensity distribution. In that framework, local positive stress changes would be associated with stronger, shear-compaction or shear-type events, where local stress relaxation areas would be associated with low-energetic tensile events, consistent with the observed differences in the frequency-magnitude distribution including the variations in *b*-value (Table S2 in the Supporting Information S1) and maximum magnitudes. Whether the relation between seismic event type and triggering provides an explanation of why patterns of aftershock sequences

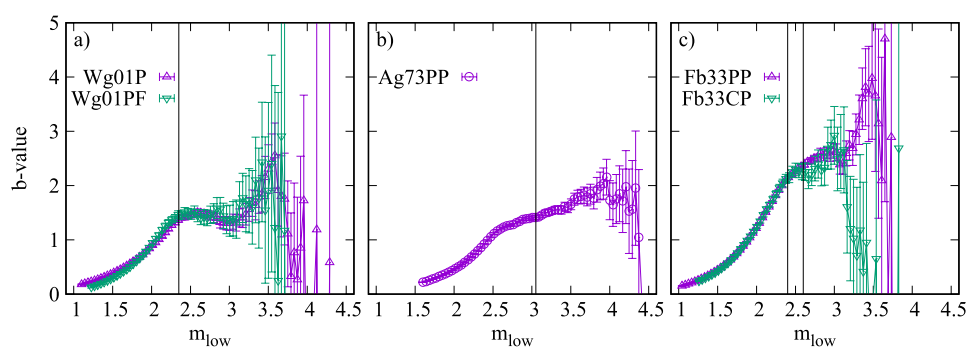


**Figure 14.** (Color online) *b*-values estimated by maximum likelihood within the interval of magnitudes $m_{low} < m < \infty$. The values for $m_{low} = m_c$ are given in Table 4.

potentially vary with mainshock faulting style (Narteau et al., 2009; Tahir & Grasso, 2015) and other mainshock attributes (Dascher-Cousineau et al., 2020), remains an open question. Upscaling our observations regarding AE kinematics and triggering to larger scales is nontrivial. The non-shear AE events are abundant at the laboratoratory scale (see, e.g., Kwiatek, Goebel, & Dresen, 2014, and references therein), and they can be explained by peculiarities of the micromechanical processes involving existing microstructure and constrained length scales. Whereas a significant portion of non-shear microseismic sources have been observed in-situ in dm-scale aftershocks following a M2 earthquake using high-frequency near-field monitoring (Kwiatek & Ben-Zion, 2013, 2016), such observations are not common at larger scales. This raises the question whether non-shear processes are less common at larger scales (change of physics or at larger scales it is easier to avoid issues of structural compatibility by having large numbers of grains available to accommodate the deformation for the same amount of bulk strain, for example), or whether this discrepancy is related to a lack of appropriate monitoring at larger scales.

### 4.2. Influence of Stress and Stress Heterogeneity on Triggering and *b*-Values

Another important finding is that triggered events exhibit a very strong tendency to have a focal mechanism similar to their trigger — with median rotation angles between 14 and 16° (Table 3). This is consistent with previous experimental findings (Davidsen et al., 2017). While this tendency could be related to optimal orientation or just local correlation in the stress field, it is important to realize that such behavior is consistent with the expectations for triggering due to static stress changes (Smith et al., 2010). This suggests that the internal stress changes leading to seismic event-event triggering in our rock samples are predominantly of static nature as it is the case for earthquakes (Hainzl et al., 2014). Whether the underlying mechanisms of the static stress changes are predominantly visco-elasticity, heat-transfer, rate-state friction, or others or a mixture thereof remains a question for the future. We would like to emphasize that given the involved time scales and the sample sizes in our experiments, our current ability to detect dynamic stress triggering is very limited. If there are any dynamically triggered events, their waveforms would be closely overlapping with that of the triggering event. In particular, their observations would be hindered by complex coda waves originating from small sample size, as well as the limited frequency band to capture much smaller events.

The significantly lower *b*-values we observe for triggered events (Figure 13) — even far from failure and similar to the case of earthquakes (Gu et al., 2013) — may originate from several processes such as dynamic effects, variations in the underlying stress field, or geometric heterogeneity (e.g., Burridge & Knopoff, 1967; Goebel et al., 2013, 2017; Mogi, 1962; Scholz, 1968a; Schorlemmer et al., 2005) and provide evidence for the potential importance of these processes in the context of triggering. These might be different from those that have been proposed for temporal variations during quasi-static and dynamic rock failure (Meredith et al., 1990), since we do not observe triggering during failure of intact rock. The combination of a pronounced similarity of focal mechanisms for triggered events together with significantly lower *b*-values, compared to background events with high *b*-value and high focal mechanism heterogeneity, is in particular consistent with previous experiments (Goebel et al., 2017; Mogi, 1962). This may indicate that the scale of the geometric or stress field heterogeneity relative to the range of AE source sizes—the scale of the micro-crack populations in our experiments is up to ≈ 3mm (Blanke et al., 2020) — governs the fraction of large-magnitude AEs and, hence, controls *b*-values as well as triggering. Yet, given that the presence of a macroscopic heterogeneity such as the saw-cut notch in experiments WgN07 and AgN01 is crucial to observe triggering — which might arise due to the increased local stress fluctuations induced by the interaction between a macroscopic crack and AE events (Kachanov, 1994) as discussed above — it is difficult to envision that stress field and geometric features beyond the scale of the micro-crack populations are more homogeneous in our experiments with a macroscopic heterogeneity than without. While heterogeneity in stress and crack orientations at smaller scales can prevent cracks from coalescing, effectively limiting larger magnitude event occurrences, high ambient (deviatoric) stresses might counterbalance this locally and give rise to both triggering and low *b*-values for triggered events. To resolve this, detailed measurements of geometrical heterogeneity and stress fields remain a challenge for the future.

Finally, we would like to emphasize that the *b*-values for the catalogs that do not exhibit triggering are not systematically different from the ones that do (Table 4 and Figure 14). Thus, the overall *b*-values alone do not allow one to identify the presence or absence of event-event triggering for the level of triggering present

in our experiments. It is conceivable though that if the fraction of triggered events is substantially higher, low $b$-values do become diagnostic for triggering.

### 4.3. Comparison With Natural Seismicity Characteristics

AE events in rock fracture also share similarities with earthquakes in tectonic settings in terms of the triggering rates associated with event-event triggering. The direct triggering rates in WgN07 follow a double power-law and the transition point between the regimes scales with the mainshock magnitude (Figure 10), consistent with findings in (Davidsen et al., 2017). The overall behavior is reminiscent of the Omori-Utsu relation in seismology (Davidsen & Baiesi, 2016; Utsu et al., 1995), the main difference being the presence of a power law for early times instead of a constant regime. The existence of the first power-law regime with an exponent $p \approx 0.7$ also holds for AgN01 and Wg01PF as our interevent time analysis shows (Figure 11). Moreover, considering an approximate equivalence between triggering rates for direct or first-generation aftershocks and all aftershocks (Helmstetter & Sornette, 2002), all values of $p$ derived from the three catalogs exhibiting triggering, and represented in Figure 11, are very similar to what has been found in other AE experiments (Baró et al., 2013; Davidsen et al., 2017; Nataf et al., 2014). Baró et al. (2013) and Nataf et al. (2014) did not observe the second power-law regime, which would imply the unphysical behavior that the number of events directly or indirectly triggered by a single event is infinite since $p \leq 1$. As shown by Baró and Davidsen (2017), it is much more likely that the second power-law regime was simply missed due to a less reliable technique to identify triggered events. In particular, having a second power-law regime with an exponent bigger than 1 ensures that the number of triggered events by a given event is finite and that a well-defined productivity relation exists. The power-law increase in average productivity with mainshock magnitude with an exponent $\alpha \approx 1.1 - 1.2$ (Figure 10) is consistent with some AE experiments (Davidsen et al., 2017) — but not with others (Baró & Davidsen, 2017) — and it is in particular consistent with what has been observed for aftershock sequences in different settings (Gu et al., 2013; Davidsen & Baiesi, 2016; Dascher-Cousineau et al., 2020; Maghsoudi et al., 2016, 2018).

Similarly, the scaling behavior including two power-law regimes of the distribution of interevent times for the catalogs exhibiting triggering (Figure 11) is consistent with what has been observed in both seismology (Bak et al., 2002; Corral, 2003) and other AE experiments (e.g., Baró et al., 2013). The existence of such scaling for a non-exponential distribution cannot be explained by a renewal model, that is, a model fully specified by a probability distribution of independent interevent times, and requires some temporal variation, or memory (Corral et al., 2008), introduced either by exogenous variations in the activity rate or by the presence of correlations between events. In our experiments showing triggering, this can be linked to triggering and large variations (or trends) in the overall rate of events. Specifically, the power-law regime for short interevent times is simply a reflection of the interevent triggering and determined by the associated triggering rate with the exponent given by $2 - 1/p$. The second power-law regime for long interevent times has often been attributed to variations over several decades in the global activity or, equivalently, a nonstationary background rate (Corral, 2003; Wheatland, 2000). As a simple example, consider the case of a Poisson process where the rate of activity grows from low values as a power-law, $\mu(t) \sim t^{1/(\nu-2)}$, within a relatively large time interval (at least one decade in $\mu$). The associated distribution of interevent times can then be approximated as $P(\delta) \sim \delta^{-\nu}$ over some range (Baró & Davidsen, 2017; Baró et al., 2013; Shcherbakov, Yakovlev, et al., 2005). This condition typically renders exponent values $\nu > 2$, with most values $2 < \nu < 3$ for faster-than-linear growths. This result is typical for AE catalogs with a smooth onset of the activity (Baró et al., 2013) such as the pre-peak activity in catalogs WgN07 and AgN01. Deviations from the power-law regime are observed for WgN07 (Figures 11a). These can be caused by a more complex evolution of the background rate, resulting in the predominance of certain temporal scales observed as a 'bump' in the decay and a lower effective exponent $\nu$. The average rate in Wg01PF also exhibits strong variations, which can be caused by changes in the background activity, rather than triggering. Such variations can explain the slight departure from the exponential tail observed in Figures 11c.

Scaling behavior together with an approximately exponential decay for long interevent times is also present in the distribution for our AE catalogs not exhibiting triggering (Figure 12). The overall interevent time distributions of the sandstone catalogs (Fb33PP and Fb33CP) are indeed close to an exponential form, while

the granite catalogs (Ag73PP and Wg01P) exhibit a clear power-law decay with an exponent of approximately 0.3 for short interevent times. Both findings are identical to other fracture experiments on sandstone and granite samples (Davidsen et al., 2007) and similar exponents have been observed under thermal driving (Xie et al., 2019) and in the uniaxial compression of different brittle materials, including artificial porous glasses (Baró et al., 2013; Nataf et al., 2014), bones (Baró et al., 2016), and wood (Alava et al., 2006). This behavior also closely resembles that observed in fracture experiments of single crystals (Åström et al., 2006), for earthquake catalogs during "stationary" periods from worldwide to local scales and for different tectonic setting (Corral, 2004, 2006, 2009) as well as in micro-, nano-, and picoseismicity induced by mining or by long-term fluid injection (Davidsen & Kwiatek, 2013).

## 5. Conclusions

Seismic aftershock triggering in rock fracture only plays a significant role in the presence of large-scale stress heterogeneities or during post-fracture stress relaxation along the newly created lab faults. Triggering is often closely related to seismic events with significant isotropic, compaction components and it leads to a strong tendency to have similar focal mechanisms and an increase in larger events. The statistical properties of seismic triggering in rock fracture closely resemble those of aftershock sequences at larger scales suggesting some degree of scale-invariance in the underlying triggering processes.

To conclude, we made four key observations related to triggerability in rock fracture: (a) Elevated stresses and seismic event localization alone as observed during crack propagation do not consistently result in aftershock triggering. (b) Post-fracture stress relaxation processes are naturally associated with aftershock triggering as well as large-scale stress heterogeneity, which locally amplifies stresses. (c) Aftershock triggering occurs both during episodes of high and low stresses, for example, elevated confining pressures. (d) Compaction and double couple events play a dominant role for event-event triggering while also constraining the focal mechanisms of the triggered events.

## Appendix A: AE Location

To locate AE events, 8–14 P-wave onset times were inverted using a simplex optimization technique and assuming a time-dependent 5-layered quasi-anisotropic velocity model (Kwiatek, Charalampidou, & Dresen, 2014; Stanchits et al., 2006). The velocity model was derived from active ultrasonic transmission measurements performed every 30 s in the course of each experiment. The resulting location accuracy was ± 2 mm (Stanchits et al., 2006).

## Appendix B: Moment-Tensor Inversion

The full moment tensor (FMT) inversion of AE data using first-motion P-wave amplitudes was performed using the fociMT application from the hybridMT software package (Kwiatek et al., 2016). The input P-wave amplitudes were corrected for coupling quality following the approach by Kwiatek, Charalampidou, and Dresen (2014). The calculated FMTs were decomposed into isotropic (ISO), compensated linear vector dipole (CLDV), and double-couple (DC) parts using the standard FMT decomposition scheme presented in (Knopoff & Randall, 1970).

## Appendix C: Bi-Test

For the Bi-Test, it is customary to test the statistical deviations from the uniform distribution by using a Kolmogorov-Smirnov (KS) test. For a large number ($N$) of $H$ values, the difference between the cumulative distribution ($F_N(H)$) and the Poisson null-model prediction ($F(H) = H$) is expected to scale with $N^{-1/2}$. $P$-values for rejection can be drawn from comparing the maximum scaled difference $\max(\sqrt{N}\,(|F_N(H) - H|))$ with a Kolmogorov distribution.

## Data Availability Statement

The data supporting the conclusions can be obtained from the associated data publication (Goebel et al., 2021) hosted by GFZ Data Services at http://doi.org/10.5880/GFZ.4.2.2020.004. All algorithms supporting the conclusions can be obtained from the references and the Supporting Information S1.

**Acknowledgments**
J. Davidsen and T. Goebel were financially supported by the Alexander von Humboldt-Foundation. J. Davidsen would like to thank the GFZ for its hospitality. G. Kwiatek acknowledges support from the Deutsche Forschungsgemeinschaft (DFG), Grant KW 84/4-1. J. Baró thanks the financial support from the AXA Research Fund through the project RheMechFail. The authors thank Ian Main and three anonymous reviewers for their helpful comments. Open access funding enabled and organized by Projekt DEAL.

## References

Alava, M. J., Nukala, P. K. V. V., & Zapperi, S. (2006). Statistical models of fracture. *Advances in Physics*, *55*(3–4), 349–476. https://doi.org/10.1080/00018730300741518

Åström, J., Di Stefano, P. C. F., Pröbst, F., Stodolsky, L., Timonen, J., Bucci, C., & Zerle, L. (2006). Fracture processes observed with a cryogenic detector. *Physics Letters A*, *356*(4–5), 262. https://doi.org/10.1016/j.physleta.2006.03.059

Bak, P., Christensen, K., Danon, L., & Scanlon, T. (2002). Unified scaling law for earthquakes. *Physical Review Letters*, *88*, 178501. https://doi.org/10.1103/PhysRevLett.88.178501

Baró, J., Corral, Á., Illa, X., Planes, A., Salje, E. K. H., Schranz, W., & Vives, E. (2013). Statistical similarity between the compression of a porous material and earthquakes. *Physical Review Letters*, *110*(8), 88702. https://doi.org/10.1103/PhysRevLett.110.088702

Baró, J., Dahmen, K. A., Davidsen, J., Planes, A., Castillo, P. O., Nataf, G. F., & Vives, E. (2018). Experimental evidence of accelerated seismic release without critical failure in acoustic emissions of compressed nanoporous materials. *Physical Review Letters*, *120*(24), 245501. https://doi.org/10.1103/PhysRevLett.120.245501

Baró, J., & Davidsen, J. (2017). Are triggering rates of labquakes universal? Inferring triggering rates from incomplete information. *The European Physical Journal — Special Topics*, *226*(15), 3211–3225. https://doi.org/10.1140/epjst/e2017-70072-4

Baró, J., & Davidsen, J. (2018). Universal avalanche statistics and triggering close to failure in a mean-field model of rheological fracture. *Physical Review E*, *97*(3), 033002. https://doi.org/10.1103/PhysRevE.97.033002

Baró, J., Martín-Olalla, J.-M., Romero, F. J., Gallardo, M. C., Salje, E. K. H., Vives, E., & Planes, A. (2014). Avalanche correlations in the martensitic transition of a Cu–Zn–Al shape memory alloy: Analysis of acoustic emission and calorimetry. *Journal of Physics: Condensed Matter*, *26*, 125401. https://doi.org/10.1088/0953-8984/26/12/125401

Baró, J., Shyu, P., Pang, S., Jasiuk, I. M., Vives, E., Salje, E. K. H., & Planes, A. (2016). Avalanche criticality during compression of porcine cortical bone of different ages. *Physical Review E — Statistical Physics, Plasmas, Fluids, and Related Interdisciplinary Topics*, *93*, 053001. https://doi.org/10.1103/PhysRevE.93.053001

Bayliss, K., Naylor, M., & Main, I. G. (2019). Probabilistic identification of earthquake clusters using rescaled nearest neighbour distance networks. *Geophysical Journal International*, *217*(1), 487–503. https://doi.org/10.1093/gji/ggz034

Ben-Zion, Y. (2008). Collective behavior of earthquakes and faults: Continuum-discrete transitions, progressive evolutionary changes, and different dynamic regimes. *Reviews of Geophysics*, *46*, RG4006. https://doi.org/10.1029/2008RG000260

Bi, H., Börner, G., & Chu, Y. (1989). Correlations in the absorption lines of the quasar Q 0420–388. *Astronomy and Astrophysics*, *218*, 19–23.

Blanke, A., Kwiatek, G., Goebel, T., Bohnhoff, M., & Dresen, G. (2020). Stress drop–magnitude dependence of acoustic emissions during laboratory stick-slip. *Geophysical Journal International*, *224*, 1371–1380.

Brodsky, E. E. (2006). Long-range triggered earthquakes that continue after the wave train passes. *Geophysical Research Letters*, *33*(15), L15313. https://doi.org/10.1029/2006GL026605

Burridge, R., & Knopoff, L. (1967). Model and theoretical seismicity. *Bulletin of the Seismological Society of America*, *57*, 341.

Charalampidou, E.-M., Stanchits, S., Kwiatek, G., & Dresen, G. (2014). Brittle failure and fracture reactivation in sandstone by fluid injection. *European Journal of Environmental and Civil Engineering*, *19*(5), 564–579. https://doi.org/10.1080/19648189.2014.896752

Corral, Á. (2003). Local distribution and rate fluctuations in a unified scaling law for earthquakes. *Physical Review E*, *68*, 035102.

Corral, Á. (2004). Long-term clustering, scaling, and universality in the temporal occurrence of earthquakes. *Physical Review Letters*, *92*, 108501.

Corral, A. (2006). Dependence of earthquake recurrence times and independence of magnitudes on seismicity history. *Tectonophysics*, *424*(3), 177–193. https://doi.org/10.1016/j.tecto.2006.03.035

Corral, Á. (2009). Statistical tests for scaling in the inter-event times of earthquakes in California. *International Journal of Modern Physics B*, *23*, 5570–5582. https://doi.org/10.1142/S0217979209063869

Corral, A., Telesca, L., & Lasaponara, R. (2008). Scaling and correlations in the dynamics of forest-fire occurrence. *Physical Review E - Statistical Physics, Plasmas, Fluids, and Related Interdisciplinary Topics*, *77*, 016101. https://doi.org/10.1103/PhysRevE.77.016101

Dascher-Cousineau, K., Brodsky, E. E., Lay, T., & Goebel, T. H. W. (2020). What controls variations in aftershock productivity? *Journal of Geophysical Research: Solid Earth*, *125*(2), e2019JB018111. https://doi.org/10.1029/2019JB018111

Davidsen, J., & Baiesi, M. (2016). Self-similar aftershock rates. *Physical Review E*, *94*(2), 022314. https://doi.org/10.1103/PhysRevE.94.022314

Davidsen, J., Gu, C., & Baiesi, M. (2015). Generalized Omori-Utsu law for aftershock sequences in southern California. *Geophysical Journal International*, *201*, 965. https://doi.org/10.1093/gji/ggv061

Davidsen, J., & Kwiatek, G. (2013). Earthquake interevent time distribution for induced micro-, nano- and picoseismicity. *Physical Review Letters*, *110*(6), 68501. https://doi.org/10.1103/PhysRevLett.110.068501

Davidsen, J., Kwiatek, G., Charalampidou, E. M., Goebel, T., Stanchits, S., Rück, M., & Dresen, G. (2017). Triggering processes in rock fracture. *Physical Review Letters*, *119*(6), 068501. https://doi.org/10.1103/PhysRevLett.119.068501

Davidsen, J., Stanchits, S., & Dresen, G. (2007). Scaling and universality in rock fracture. *Physical Review Letters*, *98*(12), 125502. https://doi.org/10.1103/PhysRevLett.98.125502

Deluca, A., & Corral, Á. (2013). Fitting and goodness-of-fit test of non-truncated and truncated power-law distributions. *Acta Geophysica*, *61*(6), 1351–1394. https://doi.org/10.2478/s11600-013-0154-9

Dresen, G., Kwiatek, G., Goebel, T., & Ben-Zion, Y. (2020). Seismic and aseismic preparatory processes before large stick–slip failure. *Pure and Applied Geophysics*, *177*, 5741–5760.

Goebel, T., Kwiatek, G., Stanchits, S., & Davidsen, J. (2021). *Source parameters of acoustic emissions from triaxial experiments on westerly granite, aue granite and flechtigen sandstone. v. 1.0*. GFZ Data Services. https://doi.org/10.5880/GFZ.4.2.2020.004

Goebel, T. H., Kwiatek, G., Becker, T. W., Brodsky, E. E., & Dresen, G. (2017). What allows seismic events to grow big? Insights from b-value and fault roughness analysis in laboratory stick-slip experiments. *Geology*, *45*(9), 815–818. https://doi.org/10.1130/G39147.1

Goebel, T. H. W., Becker, T. W., Sammis, C. G., Dresen, G., & Schorlemmer, D. (2014). Off-fault damage and acoustic emission distributions during the evolution of structurally complex faults over series of stick-slip events. *Geophysical Journal International*, *197*(3), 1705. https://doi.org/10.1093/gji/ggu074

Goebel, T. H. W., Becker, T. W., Schorlemmer, D., Stanchits, S., Sammis, C. G., Rybacki, E., & Dresen, G. (2012). Identifying fault heterogeneity through mapping spatial anomalies in acoustic emission statistics. *Journal of Geophysical Research*, *117*(3), B03310. https://doi.org/10.1029/2011JB008763

Goebel, T. H. W., Sammis, C. G., Becker, T. W., Dresen, G., & Schorlemmer, D. (2015). A comparision of seismicity characteristics and fault structure in stick-slip experiments and nature. *Pure and Applied Geophysics*, *172*, 2247.

Goebel, T. H. W., Schorlemmer, D., Becker, T. W., Dresen, G., & Sammis, C. G. (2013). Acoustic emissions document stress changes over many seismic cycles in stick-slip experiments. *Geophysical Research Letters*, *40*(10), 2049. https://doi.org/10.1002/grl.50507

Graham, C. C., Stanchits, S., Main, I. G., & Dresen, G. (2010). Comparison of polarity and moment tensor inversion methods for source analysis of acoustic emission data. *International Journal of Rock Mechanics and Mining Sciences*, *47*(1), 161–169. https://doi.org/10.1016/j.ijrmms.2009.05.002

Gu, C., Schumann, A. Y., Baiesi, M., & Davidsen, J. (2013). Triggering cascades and statistical properties of aftershocks. *Journal of Geophysical Research: Solid Earth*, *118*(8), 4278. https://doi.org/10.1002/jgrb.50306

Gutenberg, B., & Richter, C. (1949). *Seismicity of the earth*. Princeton, NJ: Princeton University Press.

Hainzl, S., Moradpour, J., & Davidsen, J. (2014). Static stress triggering explains the empirical aftershock distance decay. *Geophysical Research Letters*, *41*, 8818.

Heimisson, E. R., & Segall, P. (2018). Constitutive law for earthquake production based on rate-and-state friction: Dieterich 1994 revisited. *Journal of Geophysical Research: Solid Earth*, *123*(5), 4141–4156. https://doi.org/10.1029/2018JB015656

Helmstetter, A., & Sornette, D. (2002). Subcritical and supercritical regimes in epidemic models of earthquake aftershocks. *Journal of Geophysical Research*, *107*(B10), ESE 10-1–ESE 10-21. https://doi.org/10.1029/2001JB001580

Henderson, J., Main, I. G., Pearce, R. G., & Takeya, M. (1994). Seismicity in north-eastern Brazil: Fractal clustering and the evolution of the b value. *Geophysical Journal International*, *116*(1), 217–226. https://doi.org/10.1111/j.1365-246X.1994.tb02138

Hirata, T., Satoh, T., & Ito, K. (1987). Fractal structure of spatial distribution of microfracturing in rock. *Geophysical Journal of the Royal Astronomical Society*, *90*, 369. https://doi.org/10.1111/j.1365-246X.1987.tb00732.x

Holliday, J. R., Turcotte, D. L., & Rundle, J. B. (2008). A review of earthquake statistics: Fault and seismicity-based models, ETAS and BASS. *Pure and Applied Geophysics*, *165*(6), 1003–1024. https://doi.org/10.1007/s00024-008-0344-6

Hudson, J. A., Pearce, R. G., & Rogers, R. M. (1989). Source type plot for inversion of the moment tensor. *Journal of Geophysical Research*, *94*(B1), 765–774. https://doi.org/10.1029/JB094iB01p00765

Kachanov, M. (1994). Advanced applied mechanics: Elastic solids with many cracks and related problems. *Advances in Applied Mechanics*, *30*, 259–445. https://doi.org/10.1016/S0065-2156(08)70176-5

Kagan, Y. Y. (2007). Simplified algorithms for calculating double-couple rotation. *Geophysical Journal International*, *171*(1), 411–418.

Knopoff, L., & Randall, M. J. (1970). The compensated linear-vector dipole. A possible mechanism for deep earthquakes. *Journal of Geophysical Research*, *75*(26), 4957–4963. https://doi.org/10.1029/JB075i026p04957

Kun, F., Varga, I., Lennartz-Sassinek, S., & Main, I. G. (2014). Rupture cascades in a discrete element model of a porous sedimentary rock. *Physical Review Letters*, *112*(6), 65501. https://doi.org/10.1103/PhysRevLett.112.065501

Kwiatek, G., & Ben-Zion, Y. (2013). Assessment of P and S wave energy radiated from very small shear-tensile seismic events in a deep South African mine. *Journal of Geophysical Research*, *118*(7), 3630–3641. https://doi.org/10.1002/jgrb.50274

Kwiatek, G., & Ben-Zion, Y. (2016). Theoretical limits on detection and analysis of small earthquakes. *Journal of Geophysical Research: Solid Earth*, *121*(8), 5898–5916. https://doi.org/10.1002/2016JB012908

Kwiatek, G., Charalampidou, E.-M., & Dresen, G. (2014). An improved method for seismic moment tensor inversion of acoustic emissions through assessment of sensor coupling and sensitivity to incidence angle. *International Journal of Rock Mechanics and Mining Sciences*, *65*, 153–161. https://doi.org/10.1016/j.ijrmms.2013.11.005

Kwiatek, G., Goebel, T. H. W., & Dresen, G. (2014). Seismic moment tensor and b value variations over successive seismic cycles in laboratory stick-slip experiments. *Geophysical Research Letters*, *41*, 5838–5846. https://doi.org/10.1002/2014GL060159

Kwiatek, G., Martínez-Garzón, P., & Bohnhoff, M. (2016). HybridMT: A MATLAB/shell environment package for seismic moment tensor inversion and refinement. *Seismological Research Letters*, *87*(4), 964–976. https://doi.org/10.1785/0220150251

Lennartz-Sassinek, S., Main, I. G., Zaiser, M., & Graham, C. C. (2014). Acceleration and localization of subcritical crack growth in a natural composite material. *Physical Review E*, *90*(5), 52401. https://doi.org/10.1103/PhysRevE.90.052401

Lockner, D. (1993). The role of acoustic emission in the study of rock fracture. *International Journal of Rock Mechanics and Mining Sciences & Geomechanics Abstracts*, *30*(7), 883. https://doi.org/10.1016/0148-9062(93)90041-B

Lockner, D. A., Byerlee, J. D., Kuksenko, V., Ponomarev, A., & Sidorin, A. (1991). Quasi-static fault growth and shear fracture energy in granite. *Nature*, *350*, 39–42. https://doi.org/10.1038/350039a0

Maghsoudi, S., Baró, J., Kent, A., Eaton, D., & Davidsen, J. (2018). Interevent triggering in microseismicity induced by hydraulic fracturing. *Bulletin of the Seismological Society of America*, *108*(3A), 1133–1146. https://doi.org/10.1785/0120170368

Maghsoudi, S., Eaton, D. W., & Davidsen, J. (2016). Nontrivial clustering of microseismicity induced by hydraulic fracturing. *Geophysical Research Letters*, *43*, 10672–10679. https://doi.org/10.1002/2016GL070983

Main, I., & Meredith, P. (1989). Classification of earthquake precursors from a fracture mechanics model. *Tectonophysics*, *167*(2), 273–283. https://doi.org/10.1016/0040-1951(89)90078-4

Mäkinen, T., Miksic, A., Ovaska, M., & Alava, M. J. (2015). Avalanches in wood compression. *Physical Review Letters*, *115*(5), 055501. https://doi.org/10.1103/PhysRevLett.115.055501

Marsan, D., & Helmstetter, A. (2017). How variable is the number of triggered aftershocks? *Journal of Geophysical Research: Solid Earth*, *122*(7), 5544–5560. https://doi.org/10.1002/2016JB013807

Meredith, P. G., & Atkinson, B. K. (1983). Stress corrosion and acoustic emission during tensile crack propagation in Whin Sill dolerite and other basic rocks. *Geophysical Journal of the Royal Astronomical Society*, *75*(1), 1–21. https://doi.org/10.1111/j.1365-246X.1983.tb01911.x

Meredith, P. G., Main, I. G., & Jones, C. (1990). Temporal variations in seismicity during quasi-static and dynamic rock failure. *Tectonophysics*, *175*(1–3), 249–268. https://doi.org/10.1016/0040-1951(90)90141-T

Mogi, K. (1962). Study of elastic shocks caused by the fracture of heterogeneous materials and its relation to earthquake phenomena. *Bulletin of Earthquake Research Institute, the University of Tokyo*, *40*, 125.

Mogi, K. (2007). *Experimental rock mechanics*. London, UK: Taylor & Francis Group.

Moradpour, J., Hainzl, S., & Davidsen, J. (2014). Nontrivial decay of aftershock density with distance in Southern California. *Journal of Geophysical Research: Solid Earth*, *119*, 5518. https://doi.org/10.1002/2014JB010940
Nanjo, K. Z., Turcotte, D. L., & Shcherbakov, R. (2005). A model of damage mechanics for the deformation of the continental crust. *Journal of Geophysical Research*, *110*(7), B07403. https://doi.org/10.1029/2004JB003438
Narteau, C., Byrdina, S., Shebalin, P., & Schorlemmer, D. (2009). Common dependence on stress for the two fundamental laws of statistical seismology. *Nature (London)*, *462*, 642.
Narteau, C., Shebalin, P., & Holschneider, M. (2002). Temporal limits of the power law aftershock decay rate. *Journal of Geophysical Research*, *107*(B12), 2359. https://doi.org/10.1029/2002JB001868
Nataf, G. F., Castillo-Villa, P. O., Sellappan, P., Kriven, W. M., Vives, E., Planes, A., & Salje, E. K. H. (2014). Predicting failure: Acoustic emission of berlinite under compression. *Journal of Physics: Condensed Matter: An Institute of Physics journal*, *26*(27), 275401. https://doi.org/10.1088/0953-8984/26/27/275401
Ogata, Y. (1988). Statistical models for earthquake occurrence and residual analysis for point-processes. *Journal of the American Statistical Association*, *83*, 9. https://doi.org/10.2307/2288914
Ohnaka, M., & Mogi, K. (1982). Frequency characteristics of acoustic emission in rocks under uniaxial compression and its relation to the fracturing process to failure. *Journal of Geophysical Research*, *87*(B5), 3873–3884. https://doi.org/10.1029/JB087iB05p03873
Peng, S., & Johnson, A. M. (1972). Crack growth and faulting in cylindrical specimens of chelmsford granite. *International Journal of Rock Mechanics and Mining Sciences and Geomechanics Abstracts*, *9*(1), 37–86. https://doi.org/10.1016/0148-9062(72)90050-2
Reasenberg, P. (1985). Second-order moment of central California seismicity, 1969–1982. *Journal of Geophysical Research: Solid Earth*, *90*, 5479. https://doi.org/10.1029/JB090iB07p05479
Reches, Z., & Lockner, D. A. (1994). Nucleation and growth of faults in brittle rocks. *Journal of Geophysical Research*, *99*(B9), 18159–18173. https://doi.org/10.1029/94JB00115
Ribeiro, H. V., Costa, L. S., Alves, L. G. A., Santoro, P. A., Picoli, S., Lenzi, E. K., & Mendes, R. S. (2015). Analogies between the cracking noise of ethanol-dampened charcoal and earthquakes. *Physical Review Letters*, *115*(2), 025503. https://doi.org/10.1103/PhysRevLett.115.025503
Schmid, A., & Grasso, J.-R. (2012). Omori law for eruption foreshocks and aftershocks. *Journal of Geophysical Research*, *117*(7), B07302. https://doi.org/10.1029/2011JB008975
Scholz, C. H. (1968). The frequency-magnitude relation of microfracturing in rock and its relation to earthquakes. *Bulletin of the Seismological Society of America*, *58*(1), 399–415. Retrieved from http://www.bssaonline.org/cgi/content/abstract/58/1/399
Scholz, C. H. (1968). Microfractures, aftershocks, and seismicity. *Bulletin of the Seismological Society of America*, *58*(3), 1117. https://doi.org/10.1785/BSSA0580031117
Schorlemmer, D., Wiemer, S., & Wyss, M. (2005). Variations in earthquake-size distribution across different stress regimes. *Nature*, *437*, 539.
Shcherbakov, R., Turcotte, D. L., & Rundle, J. B. (2005). Aftershock statistics. *Pure and Applied Geophysics*, *162*(6–7), 1051–1076. https://doi.org/10.1007/s00024-004-2661-8
Shcherbakov, R., Yakovlev, G., Turcotte, D. L., & Rundle, J. B. (2005). Model for the distribution of aftershock interoccurrence times. *Physical Review Letters*, *95*, 218501. https://doi.org/10.1103/PhysRevLett.95.218501
Smith, D. E., Dietrich, J. H., & Dieterich, J. H. (2010). Aftershock sequences modeled with 3-D stress heterogeneity and rate-state seismicity equations: Implications for crustal stress estimation. *Pure and Applied Geophysics*, *167*(8–9), 1067. https://doi.org/10.1007/s00024-010-0093-1
Stanchits, S., Mayr, S., Shapiro, S., & Dresen, G. (2011). Fracturing of porous rock induced by fluid injection. *Tectonophysics*, *503*(1–2), 129–145. https://doi.org/10.1016/j.tecto.2010.09.022
Stanchits, S., Vinciguerra, S., & Dresen, G. (2006). Ultrasonic velocities, acoustic emission characteristics and crack damage of basalt and granite. *Pure and Applied Geophysics*, *163*(5–6), 974–993. https://doi.org/10.1007/s00024-006-0059-5
Stein, R. S. (1999). The role of stress transfer in earthquake occurrence. *Nature*, *402*, 605.
Tahir, M., & Grasso, J. R. (2015). Faulting style controls for the space–time aftershock patterns. *Bulletin of the Seismological Society of America*, *105*(5), 2480–2497. https://doi.org/10.1785/0120140336
Utsu, T., Ogata, Y., & Matsu'ura, S. R. (1995). The centenary of the Omori formula for a decay law of aftershock activity. *Journal of Physics of the Earth*, *43*(1), 1–33. https://doi.org/10.4294/jpe1952.43.1
van der Elst, N. J., & Brodsky, E. E. (2010). Connecting near-field and far-field earthquake triggering to dynamic strain. *Journal of Geophysical Research: Solid Earth*, *115*, B07311. https://doi.org/10.1029/2009JB006681
van Der Elst, N. J., Savage, H. M., Keranen, K. M., & Abers, G. A. (2013). Enhanced remote earthquake triggering at fluid-injection sites in the midwestern United States. *Science*, *341*(6142), 164. https://doi.org/10.1126/science.1238948
Vavryčuk, V. (2001). Inversion for parameters of tensile earthquakes. *Journal of Geophysical Research: Solid Earth*, *106*(B8), 16339–16355. https://doi.org/10.1029/2001JB000372
Vavryčuk, V. (2014). Moment tensors: Decomposition and visualization. In M. Beer, I. A. Kougioumtzoglou, E. Patelli, & I. S.-K. Au (Eds.), *Encyclopedia of earthquake engineering* (pp. 1–16). Berlin, Heidelberg: Springer Berlin Heidelberg.
Velasco, A. A., Hernandez, S., Parsons, T., & Pankow, K. (2008). Global ubiquity of dynamic earthquake triggering. *Nature Geoscience*, *1*(6), 375–379. https://doi.org/10.1038/ngeo204
Vu, C. C., Amitrano, D., Plé, O., & Weiss, J. (2019). Compressive failure as a critical transition: Experimental evidence and mapping onto the universality class of depinning. *Physical Review Letters*, *122*(1), 015502. https://doi.org/10.1103/PhysRevLett.122.015502
Wetzler, N., Brodsky, E. E., & Lay, T. (2016). Regional and stress drop effects on aftershock productivity of large megathrust earthquakes. *Geophysical Research Letters*, *43*, 12012–12020. https://doi.org/10.1002/2016GL071104
Wheatland, M. S. (2000). The origin of the solar flare waiting-time distribution. *The Astrophysical Journal*, *536*(2), L109–L112. https://doi.org/10.1086/312739
Wong, T.-f. (1982). Shear fracture energy of westerly granite from post-failure behavior. *Journal of Geophysical Research*, *87*(B2), 990–1000. https://doi.org/10.1029/JB087iB02p00990
Xie, K., Jiang, X., Jiang, D., Xiao, Y., Chen, S., Dahmen, K. A., & Salje, E. K. (2019). Change of crackling noise in granite by thermal damage: Monitoring nuclear waste deposits. *American Mineralogist*, *104*(11), 1578–1584. https://doi.org/10.2138/am-2019-7058
Zaliapin, I., & Ben-Zion, Y. (2013). Earthquake clusters in southern California I: Identification and stability. *Journal of Geophysical Research: Solid Earth*, *118*, 2847. https://doi.org/10.1002/jgrb.50179
Zaliapin, I., Gabrielov, A., Keilis-Borok, V., & Wong, H. (2008). Clustering analysis of seismicity and aftershock identification. *Physical Review Letters*, *101*(1), 18501. https://doi.org/10.1103/PhysRevLett.101.018501

Zang, A., Wagner, F. C., Stanchits, S., Dresen, G., Andresen, R., & Haidekker, M. A. (1998). Source analysis of acoustic emissions in Aue granite cores under symmetric and asymmetric compressive loads. *Geophysical Journal International*, *135*(3), 1113–1130. https://doi.org/10.1046/j.1365-246X.1998.00706.x

Zhang, X., & Shcherbakov, R. (2016). Power-law rheology controls aftershock triggering and decay. *Scientific Reports*, *6*, 36668. https://doi.org/10.1038/srep36668

Zhuang, J., Werner, M. J., & Harte, D. S. (2013). Stability of earthquake clustering models: Criticality and branching ratios. *Physical Review E*, *88*(6), 062109. https://doi.org/10.1103/PhysRevE.88.062109